



## Open Archive Toulouse Archive Ouverte (OATAO)

OATAO is an open access repository that collects the work of some Toulouse researchers and makes it freely available over the web where possible.

This is an author's version published in: <https://oatao.univ-toulouse.fr/20043>

**Official URL :** <http://dx.doi.org/10.1017/S0001924000013154>

### To cite this version :

Raghunathan, Srinivasan and Bénard, Emmanuel and Watterson, John K. and Cooper, Richard K. and Curran, Richard and Price, Mark and Yao, H. and Devine, Raymond and Crawford, B. and Riordan, David and Linton, Alan J. and Richardson, J. and Tweedie, J. Key aerodynamic technologies for aircraft engine nacelles. (2006) *The Aeronautical Journal*, 110 (1107). 265-288. ISSN 0001-9240

Any correspondence concerning this service should be sent to the repository administrator:

[tech-oatao@listes-diff.inp-toulouse.fr](mailto:tech-oatao@listes-diff.inp-toulouse.fr)

# Key aerodynamic technologies for aircraft engine nacelles

S. Raghunathan, E. Benard, J. K. Watterson, R. K. Cooper, R. Curran, M. Price, H. Yao, R. Devine and B. Crawford  
Centre of Excellence for Integrated Aircraft Technologies  
School of Mechanical and Aerospace Engineering  
Queen's University Belfast  
Belfast, UK

D. Riordan, A. Linton, J. Richardson and J. Tweedie  
Bombardier  
Belfast, UK

## ABSTRACT

Customer requirements and vision in aerospace dictate that the next generation of civil transport aircraft should have a strong emphasis on increased safety, reduced environmental impact and reduced cost without sacrificing performance. In this context, the School of Mechanical and Aerospace Engineering at the Queen's University of Belfast and Bombardier have, in recent years, been conducting research into some of the key aerodynamic technologies for the next generation of aircraft engine nacelles. Investigations have been performed into anti-icing technology, efficient thrust reversal, engine fire zone safety, life cycle cost and integration of the foregoing with other considerations in engine and aircraft design. A unique correlation for heat transfer in an anti-icing system has been developed. The effect of normal vibration on heat transfer in such systems has been found to be negligible. It has been shown that carefully designed natural blockage thrust reversers without a cascade can reduce aircraft weight with only a small sacrifice in the reversed thrust. A good understanding of the pressure relief doors and techniques to improve the performance of such doors have been developed. Trade off studies between aerodynamics, manufacturing and assembly of engine nacelles have shown the potential for a significant reduction in life cycle cost.

## NOMENCLATURE

### Symbols

$A$	area
$C$	cost
$C_D$	body drag coefficient
$C_L$	body lift coefficient
$C_x$	distance between the holes in piccolo tube
$D$	jet diameter
$D$	diameter of holes in piccolo tube
$F$	learning factor
$f$	frequency
$H$	convection coefficient
$H$	jet height
$K$	thermal conductivity of air at film temperature
$K$	coefficient in cost estimation
$M$	Mach number
$\dot{m}$	average mass flow rate, $(\rho_j A_j V_j)$
$Nu$	Nusselt number
$\dot{q}$	internal heat flux
$P_r$	Prandtl number
$Re$	Reynolds number $(\rho V D / \mu)$

<i>S</i>	arc length
<i>s</i>	jet width
<i>St</i>	Strouhal number ( $fD/V$ )
<i>T</i>	air temperature
<i>U</i>	velocity in the boundary layer at $y$
$U_c$	velocity at the edge of the boundary layer
<i>V</i>	velocity
<i>VR</i>	velocity ratio
$y$	distance in the boundary layer normal to the surface
$y^*$	wall units ( $u_y/v$ )
$\delta$	boundary-layer thickness
$\mu$	dynamic viscosity
$\rho$	density

### Subscripts

<i>a</i>	average
<i>Amr</i>	amortisation
<i>Anti</i>	anti icing
<i>Asm</i>	assembly
<i>Fab</i>	fabrication
<i>I</i>	internal
<i>J</i>	jet exit
<i>Mat</i>	material
<i>Misc</i>	miscellaneous cost
<i>NC</i>	nose cowl
<i>Sup</i>	support
<i>s</i>	surface area
SIZE	
<i>w</i>	wall

### Abbreviations:

ACARE	
BPR	engine by pass ratio
CANICE	simulation code for ice accretion
CS	certification standards
DEMARDOC	design for manufacture of aerodynamic profiles to reduce aircraft direct operating cost
DFMA	design for manufacturing and assembly
DFR	discharge flow ratio
DOC	direct operating cost
EASA	european aviation safety agency
EBU	engine built unit
FAA	federal aviation administration
FAR	federal aviation regulations
GLARE	glass-reinforced fibre metal laminate
LEBU	large eddy breakup device
MEMS	micro electro-mechanical machine
pdf	probability density function
PRD	pressure relief door
RCM	rapid cost model
RPR	ram pressure recovery
sfc	specific fuel consumption
SOAMATAS	simultaneous optimisation of aerodynamic and manufacture tolerances to reduce life cycle cost
VG	vortex generator

## 1.0 INTRODUCTION

Aerospace design is driven by customer requirements, where the customer may be thought of in the widest context as including aircraft operators, fare paying passengers, national transport systems and international treaty organisations. Current trends suggest that the design of the next generation of civil transport aircraft should place a strong emphasis on increased safety,

decreased environmental impact and reduced cost, without at the same time sacrificing performance. This may be seen in some of the designs that have either been proposed or actually come to fruition. Perhaps the prime example is the debate between larger aircraft and faster aircraft epitomised by the Airbus A380 and Boeing Sonic Cruiser designs. Only the former has progressed beyond the conceptual design phase. Other antitheses exist: transonic flight (M0.85) with a traditional swept wing versus high subsonic flight (M0.70) with a lighter, cheaper unswept wing. The latter entails a cruise time penalty but brings environmental benefits and cost savings. In the search for a viable very large aircraft design to supersede the Airbus A380, it is possible that blended wing body designs may challenge the supremacy of the traditional configuration that has dominated flight for almost ten decades. Incremental steps, syntheses or paradigm shifts in aircraft design will be facilitated by technological developments in materials, manufacturing, structures, propulsion and aerodynamics.

The square-cube rule presents a serious challenge to the development of very large aircraft, but the development of new materials and fabrication processes will open up new possibilities in the same way that GLARE has been an integral element of the design of the A380. Decades of aerodynamic research in drag reduction (passive shockwave/boundary layer control, active suction, LEBUs, riblets, MEMS) have yet to provide truly significant results, and need to be more fully integrated into the whole aircraft design process. Environmental considerations may drive aircraft operating altitudes and Mach numbers down, and we may yet see the use of turboprops on very large aircraft. Meanwhile, Boeing is developing the 787, which will operate more systems electrically, with significant weight savings.

A nacelle (Fig. 1) is a key system of aircraft and typically consists of an inlet cowl, fan cowl, thrust reverser, core cowl and primary exhaust nozzle. Its primary purpose is to provide a smooth aerodynamic fairing for the power plant, while also ensuring a smooth airflow into the engine. A nacelle also houses several safety and environmental protection systems. In this context, the School of Mechanical and Aerospace Engineering at the Queen's University of Belfast (QUB) and Bombardier have, in recent years, been conducting research into some of the key aerodynamic technologies and cost analyses for the next generation of aircraft engine nacelles. Investigations have been performed into anti-icing technology, efficient thrust reversal, engine fire zone safety, noise attenuation, integration with the wing and life cycle cost optimisation with other considerations in engine and aircraft design. Some of the findings from these research activities are reported in this paper.

## 2.0 ANTI-ICING<sup>(1-34)</sup>

For an aircraft to meet safety regulations (expressed as certification requirements)<sup>(1,2)</sup> for flight into icing conditions, it must be protected against the formation of ice. Ice can cause impact damage to the aircraft structure and systems and/or performance degradation effects due, for example, to its influence on the wing aerodynamics. Lift can be reduced dramatically in conjunction with very large increase of the drag. The requirements for wing and engine installation on an aircraft, as set out in the relevant US Federal Aviation Regulations (FAR) and European Aviation Safety Agency (EASA) Certification Standards (CS), are typically met by providing the forward lip skin of each vital surface with a hot air anti-icing system (Fig. 2). A hot air system ensures that even a minimum thickness of ice can be prevented from forming on the external surface; a performance level that cannot be reached with a pneumatic boot system. Other systems present some limitations in the form of performance loss or energy cost<sup>(3)</sup>.

The general principle of the hot air system is that it takes high temperature air from the engine compressor and directs it forward

onto the inner lip skin surface to evaporate impinging water or melt accreted ice on the outer side of the skin, limiting finally the formation of ice. A preferred method of directing the hot air onto the inside skin of the forward lip is through the use of a piccolo tube (Fig. 2), though other methods, having varying degrees of effectiveness, may be used. The piccolo system utilises the effect of multiple steady hot jets impinging on the surface and interacting in various ways, thereby efficiently heating the inner surface.

In an effort to support the objectives of the FAA Icing Plan and facilitate Bombardier in the certification process, the School of Mechanical and Aerospace Engineering at QUB in conjunction with Ecole Polytechnique, Montreal has been involved with the development of reliable ice accretion and anti-icing prediction methods. The effect of engine vibration and possibility of enhancement of heat transfer by pulsejets were also considered in these studies.

## 2.1 Heat transfer correlation for piccolo systems, based on experiments<sup>(3-10)</sup>

The performance of the piccolo anti-icing system at a given flight condition depends on several factors. These include the mass flow rate, temperature drop between the engine compressor and piccolo tube, the amount of water catch, the impinging limits on the nacelle surface and the conditions for thermal equilibrium at the nose cowl surface. The critical aspect of design of an anti-icing system is the prediction of the heat transfer of the impinging jets from the piccolo tube.

There is evidence to indicate that for a single jet impinging on a surface the maximum heat transfer at the stagnation point occurs on the impingement surface when the distance between the jet and the plate is approximately equal to the length of the potential core of the jet (5-7 times the jet diameter) and heat transfer decreases for distances greater than this length. Experiments<sup>(3,10)</sup> on hot/cold air jet impingement on flat surfaces address key issues such as the effects of jet diameter, orientation, Reynolds number, jet nozzle-to-nozzle distance and jet nozzle-to-surface spacing on flow and heat transfer on flat plates. The flat plate arena has been thoroughly investigated and empirical relations have been developed that address the key issues mentioned above. However, it is very rare to find studies that have been dedicated to more complex situations such as the interaction of an impingement jet and a curved surface<sup>(7,9)</sup>.

Experiments were conducted in the QUB 1.14m x 0.85m wind tunnel of a full scale anti-icing system of an engine nacelle. The external airflow velocity and temperature were maintained at 40ms<sup>-1</sup>, and 300K, respectively. The piccolo tube had three rows of holes. The mean airflow flow temperature and velocity at the jet exit were typically 600K and 340ms<sup>-1</sup>, respectively. Tests were performed for several values of jet hole diameter, the spacing between the holes and the distance between the jet exit and the impinging surface. Based on these experiments a unique correlation for impingement heat transfer was developed (Fig. 3). The correlation is independent of hole diameter, number of holes, and the distance between the holes and the impingement surface. It depends mainly on mass flow per unit area and weakly on jet spacing, expressed as a multiple of hole diameter. (The values defining the correlation have been withheld for commercial reasons.)

## 2.2 Simulation of ice accretion<sup>(11-34)</sup>

Simulation codes for ice accretion in both two-dimensional<sup>(13-19)</sup> and three-dimensional<sup>(26)</sup> versions (CANICE) have been developed at the Ecole Polytechnique, Montreal. The development of CANICE has been geared towards the specific needs of Bombardier. Presently, a basic model for a hot-air anti-icing system is being used in CANICE. In this model, hot air from the engine is assumed

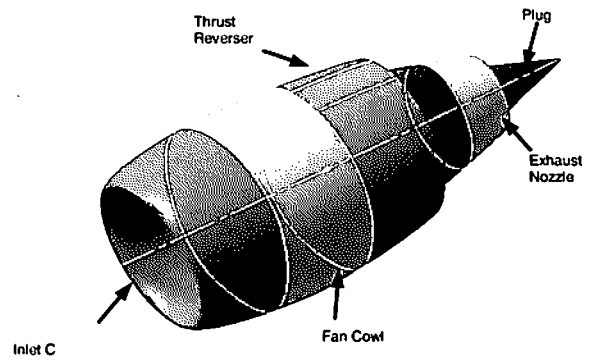
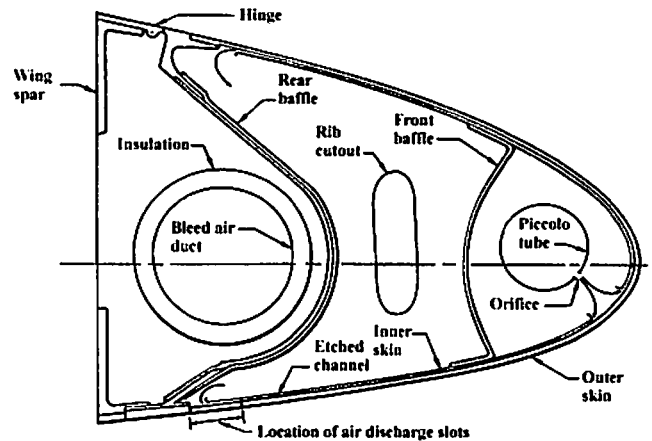
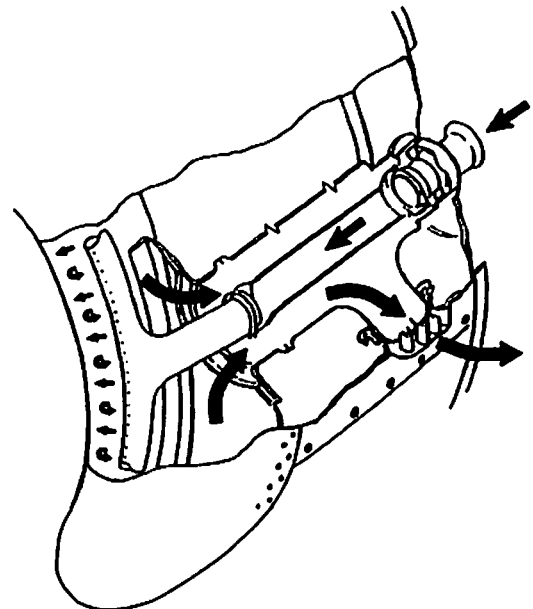


Figure 1. A nacelle.



(a) Piccolo and jets.



(b) Bleed system.

Figure 2. Piccolo anti-icing system.

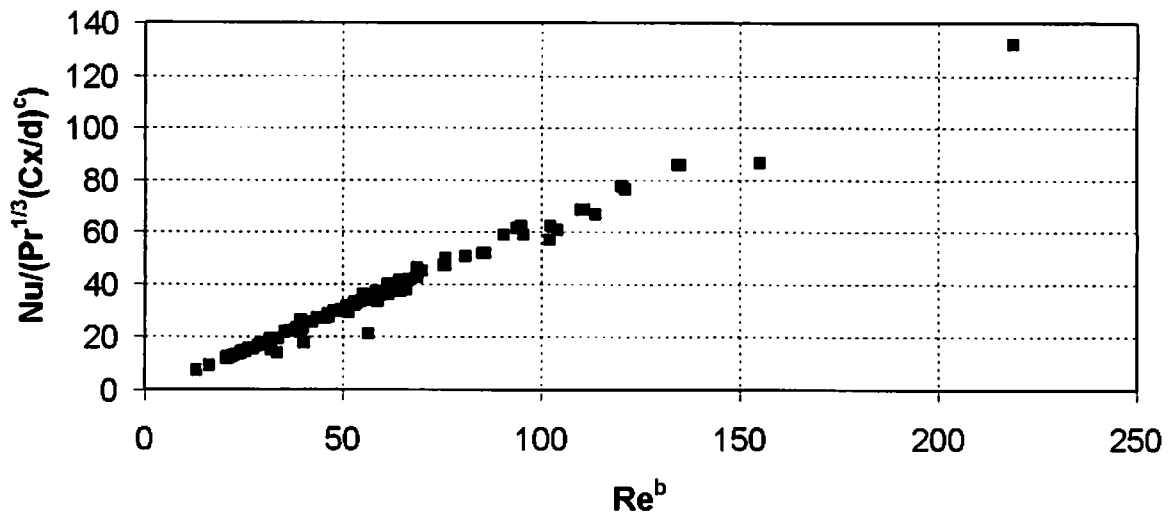


Figure 3. Unique correlation for heat transfer in anti-icing system ( $b$  and  $c$  are indices).

to impinge upon the inner surface of the aerofoil leading edge or the slat (Fig. 4). The inner region is modelled with a local internal convection coefficient  $h_{anti}$  which is considered to be known a priori. The heat flux  $\dot{q}$  from this region is then evaluated with the help of the internal hot-air temperature  $T_i$  and the local wall temperature  $T_w$ .

$$\dot{q} = h_{anti} (T_i - T_w) \quad \dots (1)$$

A limitation of this method is that the internal heat flux  $\dot{q}$  or the convection coefficient  $h_{anti}$  and temperature  $T_i$  are based on empirical relations<sup>(6)</sup> for a hot-air jet impinging on a flat plate. This has been a commonly accepted practice in studies related to anti-icing system modelling<sup>(11-25)</sup>. It must be pointed out that this local distribution of internal heat flux  $\dot{q}_i$  or the convection coefficient  $h_{anti}$  is based purely on the local distribution on a flat plate and, therefore, does not account for the curvature of the internal wall region of an aerofoil leading-edge or the wing slat. Another limitation of such a model is that it fails to provide an accurate estimate of the hot-air flux requirements and the

drain on the engine power as a result of operating the hot-air anti-icing system.

The first step towards achieving an optimum design of a hot-air anti-icing system is the development of a reliable database, experimental and numerical, related to the heat transfer from a single jet or an array of jets impinging on a curved surface. Recent studies<sup>(27,28)</sup> on the usefulness of the empirical relations developed for hot-air jet impingement on a flat surface for a highly curved two-dimensional (2D) surface showed that the flat-plate empirical relations are inadequate for predicting heat transfer on curved surfaces. Figures 4 and 5 present some results of the numerical simulation of a hot-air jet impingement on a concave surface for a 2D case. Here,  $Re_s$  is the Reynolds number based on the arc length  $s$ , and  $H$  and  $S$  are the jet height and width, respectively. As evident from Fig. 5, the most important conclusion drawn from these studies is that the flat plate correlations are not reliable enough for predicting heat transfer on a concave surface. To overcome this limitation, a numerical correlation was developed for the 2D case<sup>(28)</sup> and is now being used in the 2D version of the CANICE code.

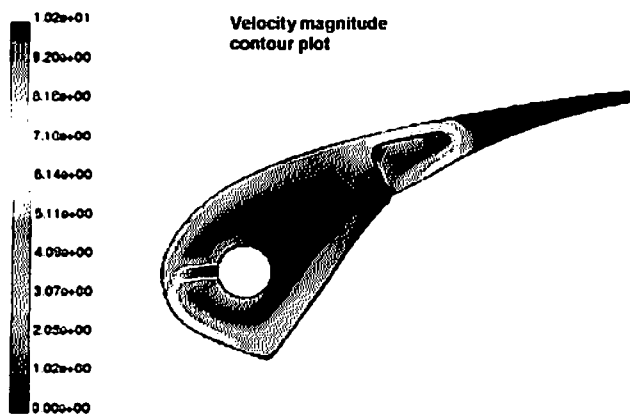


Figure 4. Numerical simulation of a hot-air jet impingement inside a slat.

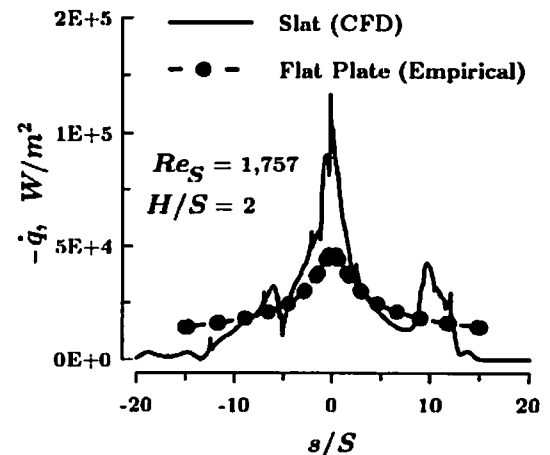


Figure 5. Comparison of the heat flux distribution ( $\dot{q}$ ) on the surface of a slat and a flat plate  $Re_s = 1,757$ .

### 2.3 Effect of normal vibration on heat transfer<sup>(35-50)</sup>

Vibration of anti-icing systems can arise from the vibration of the aircraft structure, possibly due to unsteady flow caused by ice formation. In spite of the obvious importance of potential effects on heat transfer on boundary layers, there is still only a limited experimental database available with respect to the effects of vibration on a turbulent boundary layer.

An early study by Izzo<sup>(35)</sup> suggests minor changes in mean velocity profile when compared with a non-vibrating case and that the excitation of the surface in a fundamental mode only disturbs a small portion of the energy spectrum rather than resulting in a broad disturbance of turbulent properties. A possible interpretation of this would be a strong correlation between the surface motion and the activity of the high/low velocity streaks and the coherent structures responsible for turbulence production in the near wall region of an unperturbed boundary layer<sup>(36)</sup>.

Studies have been conducted into the effects of a spanwise wall vibration<sup>(37-39)</sup> on near wall turbulence. These show a decrease in near wall turbulence due to an interaction between longitudinal vortices and the near wall high/low velocity streaks.

The influence of longitudinal vibrations, which include travelling waves, has also been investigated in relation to boundary layer transition control by compliant walls<sup>(40,41)</sup>. In this case a combination of stream-wise and longitudinal wall motions produced a very complex near wall turbulence structure. However, no significant effect on skin friction was observed. From an aero-acoustic viewpoint, several similar investigations have been carried out ranging from studies of the acoustic near field from a jet engine to turbulent boundary-layer excitation and induced skin vibrations<sup>(42-45)</sup>. It is understood from these investigations that the structure of the turbulent boundary-layer may depend on the directions of vibration and it is important to conduct controlled experiments to fully understand the effect of vibration in a particular direction on the structure of the boundary layer. This implies a strict control regime over any form of surface motion in order to isolate the specific flow effect due to an individual vibration mode.

The purpose of the investigation performed at QUB was to assess the specific effect of a wall normal vibration on a turbulent boundary layer while minimising longitudinal, spanwise and travelling wave motions. In order to assess the effect of vibration excitation in a single direction on turbulent boundary layers and heat transfer, experiments were conducted with a zero pressure gradient turbulent boundary layer on a flat plate in a low speed wind tunnel (Fig. 6)<sup>(50)</sup>. The turbulent boundary layer over the relatively short flat plate (690mm) was triggered by sand paper placed over the first 150mm of the plate. Hot wire anemometry was used to survey mean and fluctuating stream-wise velocity components and the post-processing of data involved the use of a triple decomposition algorithm. The unsteady component represents the input disturbance frequency imposed on the plate through a shaker and the fluctuating component. After the input signal has been decomposed a phase averaged cycle can be rebuilt which allows velocity profiles, turbulence profiles and frequency information to be extracted for given phase locations.

Figures 7 and 8 show typical results for velocity and turbulence profiles for the above case. The results shown here are for plate vibrating frequencies of 30Hz and 80Hz and at an amplitude of vibration of 0.76 times the boundary-layer thickness. The velocity profiles (Fig. 7) over a phase averaged cycle 'converge' into one profile and this is not significantly different from a typical turbulent boundary-layer profile<sup>(46-48)</sup>. Identical behaviour is also observed for the turbulence intensity data (Fig. 8). These results suggest that the effect of normal vibration is negligible.

Figure 9 shows a typical power spectrum for the plate, derived from an accelerometer mounted beneath the measurement position, and velocity spectra from boundary layer measurements. The results shown here are for a plate vibration of 80Hz. The accelerometer measurements on the plate show the excitation frequency of 80Hz

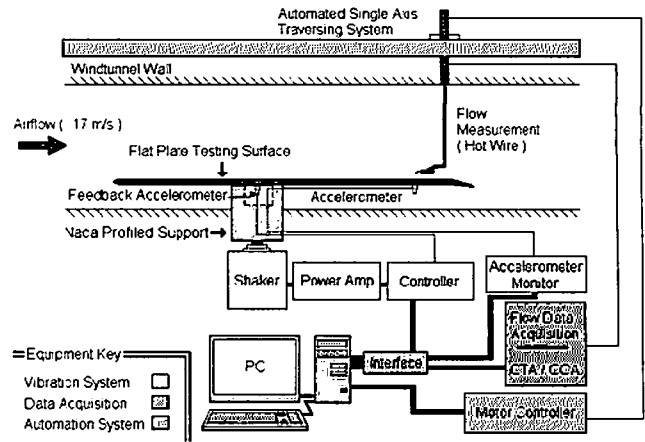


Figure 6. Test set up for vibrations.

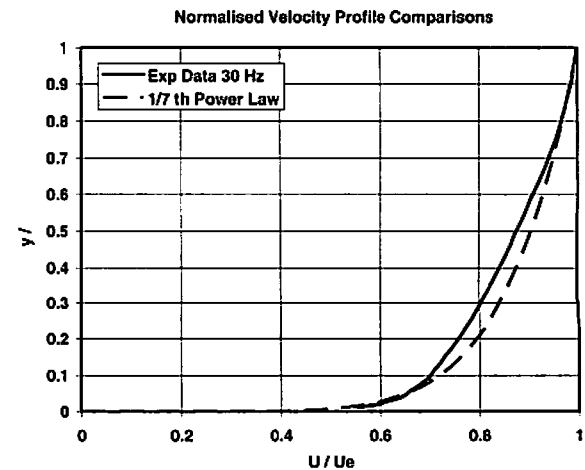
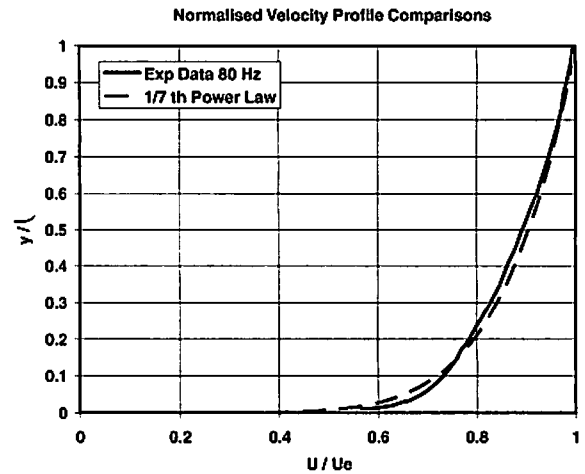
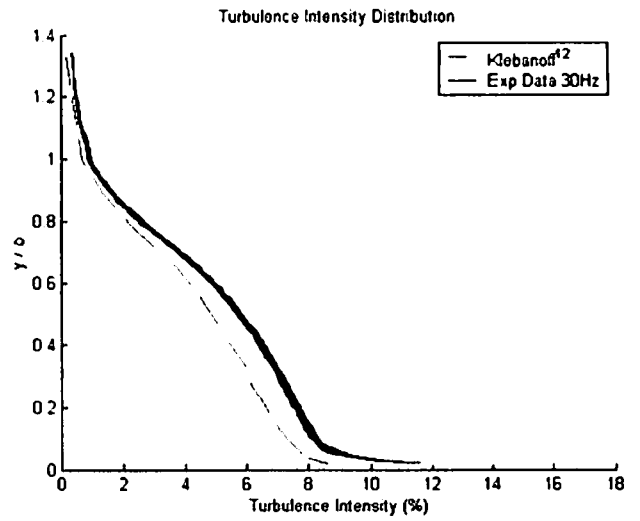
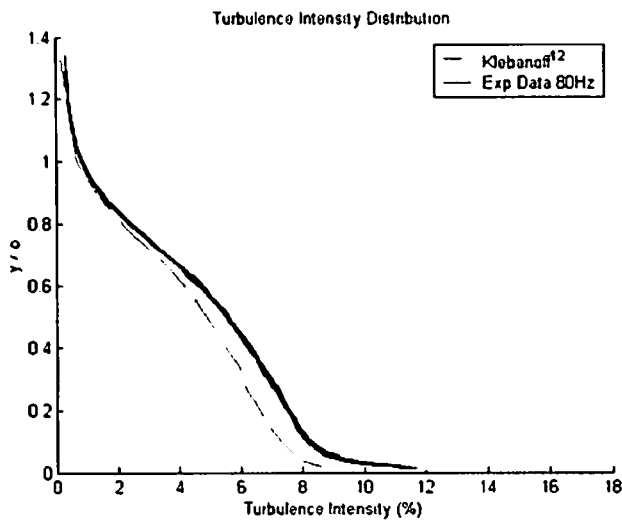


Figure 7. Normalised Mean Velocity Profile Plots for a 30Hz and 80Hz sinusoidal vibration with 2mm pk-pk amplitude, over one rebuilt phase averaged cycle. Both figures contain 300 separate boundary layer profiles representing 1-2° intervals from 0° to 360°.



Figures 8. Turbulence intensity plots for a 30Hz and 80Hz sinusoidal vibration with 2mm pk-pk amplitude, over one rebuilt phase averaged cycle. Both figures contain 300 separate turbulence profiles representing 1-2° intervals from 0° to 360°

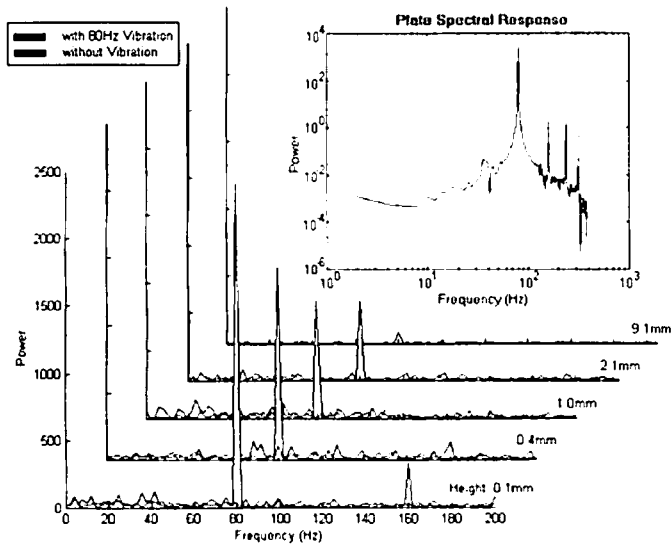


Figure 9. Boundary-layer response to plate vibrations.

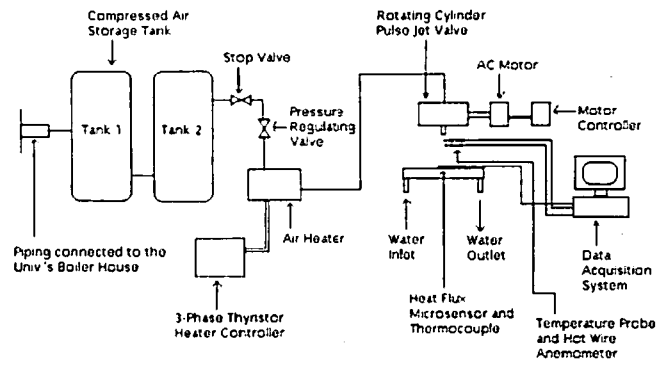


Figure 10. Schematic diagram of the experimental test set-up for pulse jets.

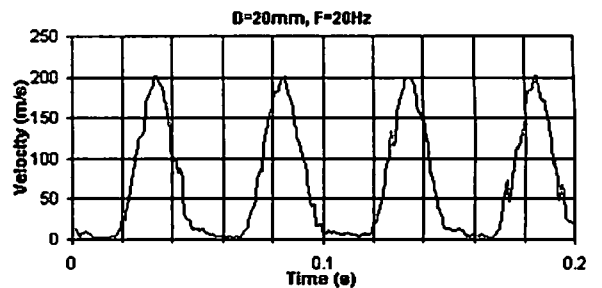
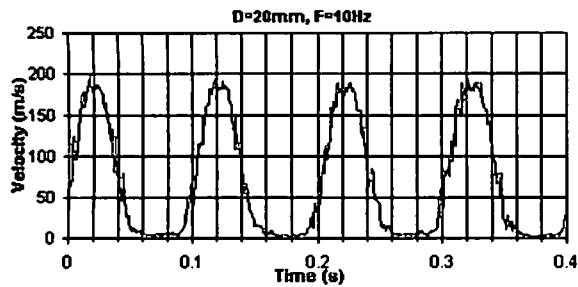


Figure 11. Velocity profile for pulse frequencies of 10 and 20Hz.

and several harmonics. The boundary layer results show that the disturbances propagate through at the plate excitation frequency and the second harmonic only. These plots highlight the fact that the boundary layer exhibits a very narrowband response to the vibration, located solely around the input frequency and its associated second harmonic.

The results also showed that the displacement thickness exhibits some phase shift, suggesting that the boundary layer does not react instantaneously to the sudden change in wall position; instead there is a delay. When probability density distributions are considered no significant change between the vibrating cases and the stationary one was observed. Finally it can be deduced that within the range of tests conducted, although the boundary layer responds to normal vibration, the effects on the velocity and turbulence profiles are very small. It could be argued therefore, that the effect of normal vibration on heat transfer is negligible and normal vibration of an engine is not a key design parameter of an aircraft anti-icing system. However, further study is required, since these observations from laboratory experiments may not be consistent with data from aircraft flight testing.

## 2.4 Effect of pulsing the jets on heat transfer<sup>(51-59)</sup>

Heat transfer in pulsating jet flows has been the subject of renewed interest in recent years in an effort to enhance the performance of the many industrial applications that use hot or cold jets. The purpose of the investigations at QUB was to assess the current understanding of the effect of pulsing a hot jet on impingement heat transfer with reference to anti-icing applications.

Test carried out by Nevins and Ball<sup>(51)</sup> on heat transfer between a flat plate and a pulsating jet showed that no significant heat transfer enhancement was obtained by using a pulsed air jet. The test was conducted at  $1,200 < Re_G < 120,000$ ,  $10^{-4} < St < 10^{-2}$ , and nozzle to plate spacing from 8 to 32 nozzle diameters. The average Reynolds number  $Re_G$  was calculated based on the average mass flow rate for each test frequency, and corresponding Strouhal number  $St$  determined using Equation (2):

$$Re_G = \frac{\dot{m}D}{A\mu} \quad St = \frac{fD\rho A}{\dot{m}} \quad \dots (2)$$

where,  $\dot{m}$  is the average mass flow rate calculated from the jet exit velocity profile,  $D$  is the nozzle diameter,  $A$  is the nozzle area,  $\mu$  is dynamic viscosity and  $\rho$  is density of air at supply air temperature, and  $f$  is pulsation frequency.

Nevins and Ball<sup>(51)</sup> did not document the extent of secondary flow structures in their experiments. Further, the experiment was studied at a very low Strouhal number which might have affected the ability to demonstrate pulsed flow heat transfer enhancement.

Kataoka and Suguro<sup>(52)</sup> show that stagnation point heat transfer for axisymmetric submerged jets is enhanced by the impingement of large-scale structures on the boundary layer, such as vortex rings which occurred in pulse flow. Further tests carried out by Sailor *et al*<sup>(53)</sup> on the effect of duty cycle variation on heat transfer enhancement for an impinging air jet showed significant heat transfer enhancement.

Mladin and Zumbrunnen<sup>(54)</sup> investigated theoretically the influence of pulse shape, frequency and amplitude on instantaneous and time-averaged convective heat transfer in a planar stagnation region using a detailed boundary layer model. They reported that there exists a threshold Strouhal number,  $St > 0.26$  below which no significant heat transfer enhancement was obtained. Results obtained by Zumbrunnen and Aziz<sup>(54)</sup> on the effect of flow intermittency on convective heat transfer to a planar water jet impinging on a constant heat flux surface reinforces this finding. This experiment carried out at  $St > 0.26$  found that local Nusselt number increases by up to 100%. However, Sailor *et al*<sup>(53)</sup> used Strouhal numbers between 0.009 and 0.042 and still recorded significant enhancement in stagnation point heat transfer for pulse flow.

Azevedo *et al*<sup>(56)</sup> investigated impingement heat transfer using a rotating cylinder valve for a range of pulse frequency. The results showed that heat transfer degraded for all frequencies. In their experiments, the velocity profile of the pulse jet shows the existence of a two-peak region for every flow cycle. This results in disturbance to the pulse flow and affects the flow structure and heat transfer. The dependence of pulse characteristics on convective heat transfer was discussed by Mladin and Zumbrunnen<sup>(55)</sup>.

Farrington and Claunch<sup>(57)</sup> carried out a test to determine the influence of flow pulsations on the flow structures of a planar jet at  $Re = 7,200$  and  $0 < St < 0.324$ . The results of the test were captured using infrared imaging and smoke-wire visualisation. They concluded that for pulsating jets, the vortices were larger than the steady jet and occurred closer to the nozzle. These larger vortices resulted in an increased entrainment and led to a wider angle of the potential core. Jets with large amplitude of pulsations entrained surrounding fluid more rapidly and decayed more quickly than steady jets. An increase in turbulence intensity can be associated with the pulse decay.

Thus results of investigations to date on the effect of pulsing a jet on heat transfer are conflicting. When compared with steady jets, some of the work shows that a pulse jet increases the heat transfer whereas other tests show that the pulse jets reduce heat transfer. In order to understand further the effect of pulse jets on heat transfer and to address the contradictions in results to date, experiments were performed<sup>(59)</sup> for both steady jets and pulsating jets at QUB.

Figure 10 shows the schematic diagram of the experimental test set-up. A vortex flow meter is placed just downstream of the pressure regulator and is used to measure the mass flow of the air jet impinging on the surface of the lip-skin. A Secomak model 15/2 air heater is used to heat the air jet. The maximum air temperature was 570K. The pulse air jet is generated using a rotating cylinder valve driven by an electric motor controlled by an electronic motor controller. Heat transfer coefficients were calculated from the value of temperature drop between the jet exit air and the lip-skin surface. Time-averaged velocity of the centreline jet exit air close to the nozzle was measured with a calibrated hot wire anemometer. A sampling frequency of 1kHz was considered adequate to capture the time variations.

The heat flux of the heated air jet impinging on the plate was measured using a heat flow and integral thermocouple sensor from RdF Corporation. The values of heat flux and plate temperature for the stagnation point and for local measurements at different radial positions were monitored and recorded by the data acquisition system. Local heat transfer measurements were recorded at radial distances from one to six nozzle diameters. The local Nusselt number was calculated using Equation (3):

$$Nu = \frac{q''D}{(T_j - T_w)k} \quad \dots (3)$$

Where  $q''$  is the stagnation point heat flux measured by the sensor,  $D$  is the nozzle diameter,  $k$  is the thermal conductivity of the air jet evaluated at film temperature,  $T_j$  is the temperature of the hot air jet and  $T_w$  is the temperature of the plate at the stagnation point. The average Nusselt number based on the local temperature difference was calculated by numerically integrating the heat flux measurement over the impingement area. The uncertainty in the heat flux measurement is estimated at 5%.

The tests were conducted<sup>(59)</sup> in the pulse frequency range of 10 to 80Hz and Reynolds number based on the jet diameter in the range 16,000 to 32,000. The nozzle to plate spacing,  $x/D$  was fixed at 4. The duty cycle of the pulse airflow, that is the fraction of time in a pulse cycle during which there was jet flow, was 0.33.

Figure 11 shows the velocity profile at pulsation frequencies of 10 and 20Hz for a jet nozzle diameter of 20mm. The ON part of the pulsation duty cycle has a velocity variation similar to a half-cycle of a sinusoid and the velocity at the nozzle exit is close to zero during



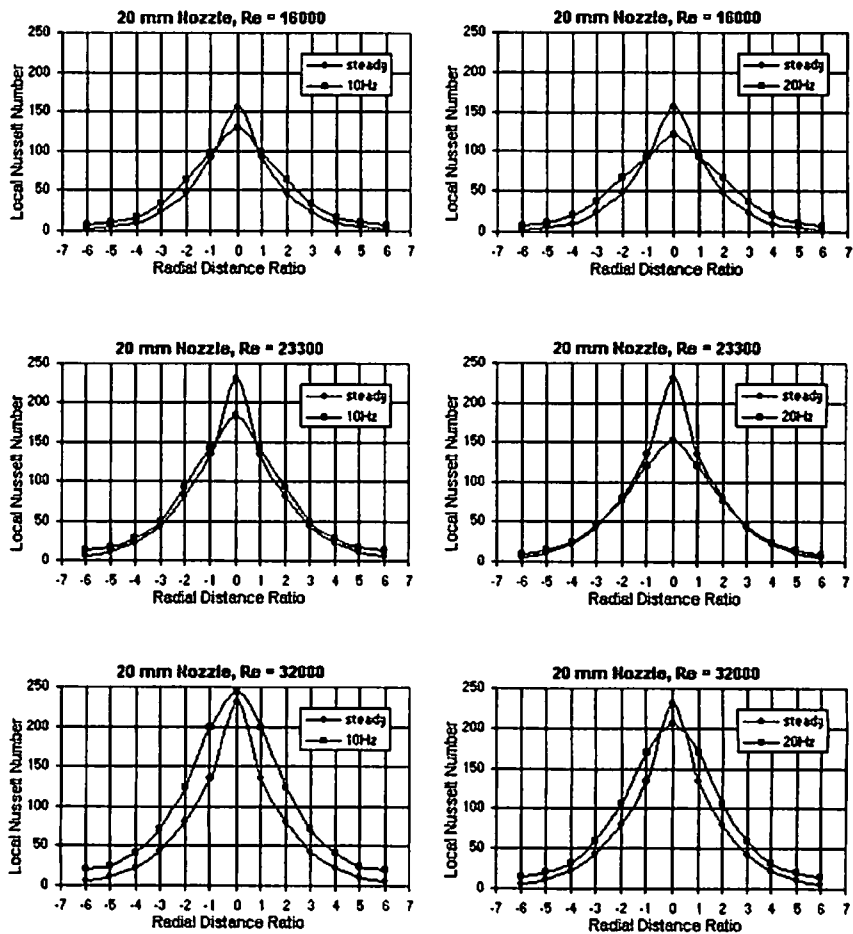


Figure 12. Variation of local Nusselt numbers with radial distance at frequencies of 10 and 20Hz for  $Re_{G_1} = 16,000, 23,300$  and  $32,000$ .

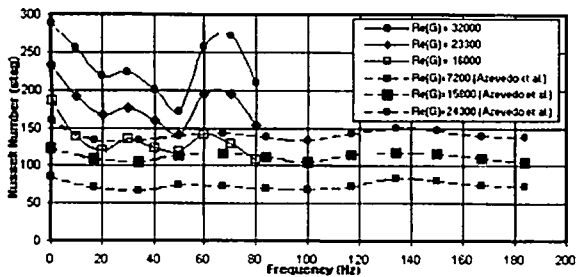


Figure 13. Variation of stagnation Nusselt numbers with frequency for Reynolds number of 16,000, 23,300 and 32,000. Comparison of current results with Azevedo *et al.*

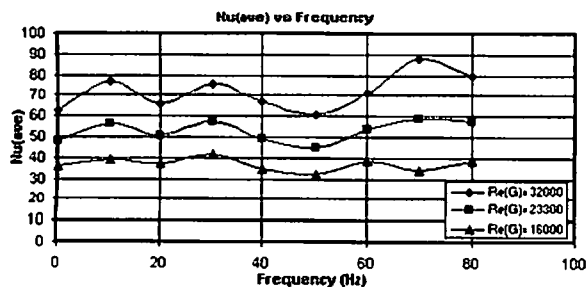
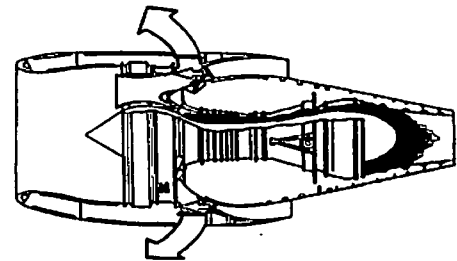
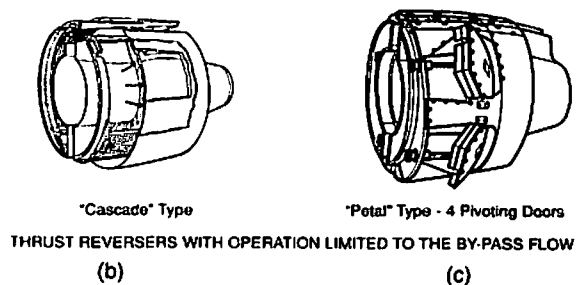


Figure 14. Variation of Nusselt numbers averaged over the impingement area with frequency for Reynolds Number = 16,000, 23,300 and 32,000.



(a) Concept of thrust reversal.



(b) (c) types of thrust reversers.

Figure 15. Thrust reverser.

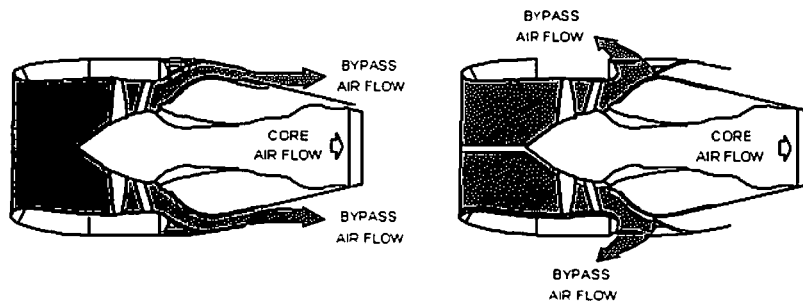


Figure 16. Schematic diagram of natural blockage thrust reverser.

the nominally OFF part of the duty cycle. This shows minimal air leakage in contrast with the work carried out by Azevedo *et al.*<sup>(56)</sup> where the leakage is quite significant. The stable flow structure created in the experiment is important in order to measure the instantaneous heat transfer correctly.

Figure 12 shows typical graphs of local Nusselt number against radial distance for frequencies of 10Hz and 20Hz for all the three Reynolds numbers under investigation. The graph shows that the local Nusselt numbers for pulse flow are higher than for steady flow at positions from 1-diameter outwards. Higher turbulence intensity at these positions is believed to contribute to the increase in heat transfer.

Figure 13 shows the dependence of stagnation Nusselt number on frequency for three Reynolds numbers at . For stagnation point heat transfer, jet pulsation has the effect of decreasing the heat transfer for all the frequencies studied. The highest frequency degradations are between 20 to 50Hz and above 80Hz. This generally is in agreement with the results obtained by Azevedo *et al.*<sup>(56)</sup>. In their experiments, where the Reynolds numbers were less than 25,000, the heat transfer results at all frequencies showed significant degradation. The results show that higher mass flow rate can influence the heat transfer measurements.

Figure 14 shows the variation of Nusselt number averaged over the impingement area with pulsed frequency  $f$ , for jet Reynolds numbers at 16,000, 23,300 and 32,000. The flow structure changes with frequency in a complex manner so the Nusselt number versus frequency curve shows no clear trend. The average Nusselt numbers for the pulse jet are equal or higher than the steady jet for all the frequencies tested except at 50Hz. The maximum average heat transfer enhancement occurs at a frequency of 70Hz for a Reynolds number of 32,000. The enhancement of heat transfer at this frequency is approximately 40%.

It should be noted that the present results were obtained at non-dimensional distance,  $x/D$  equal to four while those obtained by Azevedo *et al.*<sup>(56)</sup> were at six. This explains why a higher stagnation heat transfer value was obtained here.

The present results show that the average heat transfer on the impingement area is enhanced for almost all of the pulse frequencies investigated even though the stagnation point heat transfer decreases. These increases are shown to be available for a system that uses a single pulse jet impinging on an area with radius up to six times the nozzle diameter.

The results of the experiments show that there is significant enhancement in the local heat transfer of the pulse flow at positions one nozzle diameter or more away from the stagnation point for all the pulse frequencies. The stagnation point heat transfer does not show any enhancement for the three Reynolds numbers investigated. The average Nusselt number for the pulse jet is enhanced for all the frequencies investigated except at 50Hz. The degree of enhancement is in the range 0-40% with the greatest benefit at frequency of 70Hz for  $Re = 32,000$ .

Heat transfer in the pulse flow mode is complex and dependent on the flow structure of the jet. The significant enhancement of the heat

transfer at local distances away from the stagnation point resulted in higher average Nusselt numbers for pulse flow compared to steady flow. Significant turbulence intensity caused by pulsating the jet resulted in the increase recorded. The degradation in heat transfer at the stagnation point is believed to be due to small turbulent intensities of the pulse flow at this position.

When compared with a steady jet system a pulse jet anti-icing system could produce an enhancement in heat transfer of 10-20% or reduce the bleed air requirements by 10-20%.

### 3.0 THRUST REVERSER<sup>(60-77)</sup>

Typically on modern aircraft the thrust reverser is built into the engine nacelle (Fig. 15). A thrust reverser uses the power of a jet engine as a deceleration force by reversing the direction of exit airflow, which generates forward thrust. Fig. 15(a) shows a section through a jet engine with a typical cold stream thrust reverser. Some of the thrust reversers employ a cascade to enhance the turning of the flow<sup>(60)</sup>. There are broadly two types of thrust reversers: (a) operating on both core and fan flow; and (b) operating on the fan flow only. Thrust reversers operating on the fan flow could be cascade or petal type (Figs 15(b) and (c)).

A thrust reverser offers a number of operational advantages<sup>(60,61)</sup> shortening of landing runs, less wear and tear of aircraft brakes, safer landing in adverse weather conditions, additional safety and control margins during aborted take-offs. Thrust reversers significantly affect the nacelle design, increasing weight and resulting in higher manufacturing and operational costs.

#### 3.1 Natural blockage thrust reverser

One of the newer types of thrust reverser that operates on the fan flow is the natural blockage concept, first implemented on an aircraft by Bombardier (Fig. 16). This design concept has the potential to be more reliable and maintainable than other types of thrust reverser, since it has fewer moving parts, notably no blocker doors or links. The Bombardier natural blockage thrust reverser design for the CRJ700/900 has increased reverse thrust efficiency, allowing the engine to run slower in reverse mode. It also has a novel counter-balance mechanism, which eliminates the need for powered door operation. Studies on a natural blockage thrust reverser have found that the flow entering the fan duct is presented with a rapid expansion, while the reverser is fully deployed. This occurs just as the flow is accelerating around the curved surface of the diverter fairing. The combination of rapid expansion and high rate of turning results in flow separation. However, this separation point does not occur at a steady point, and instead moves up and down the diverter fairing surface as the trans-cowl cavity pressure rises and falls in a cyclic fashion. The resultant pressure fluctuations could have an adverse effect on the structure fatigue life, and therefore need to be taken into account in the design process.



Figure 17. The unstructured grid.

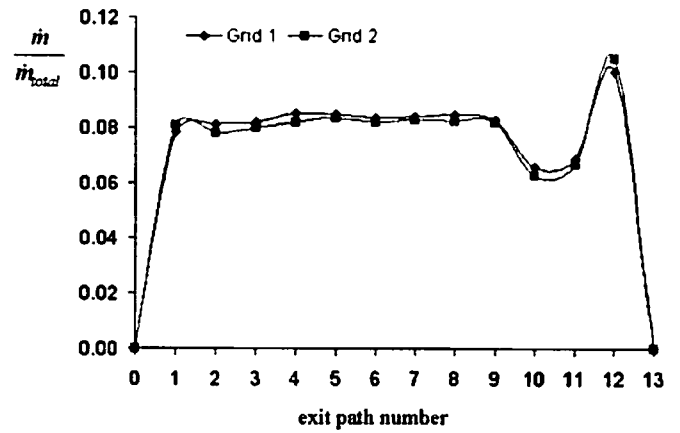


Figure 18. Normalized mass flow rate distributions of approaching the fan duct flow to the cascade.

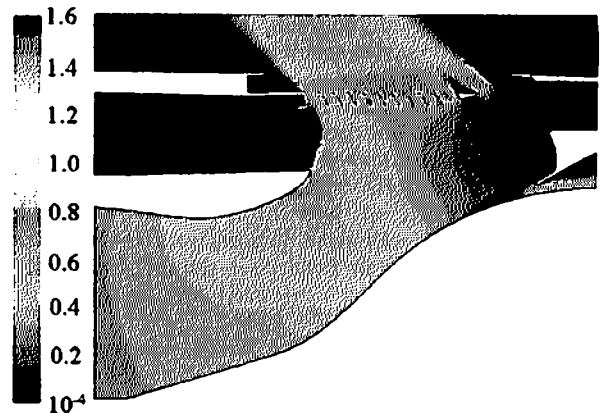
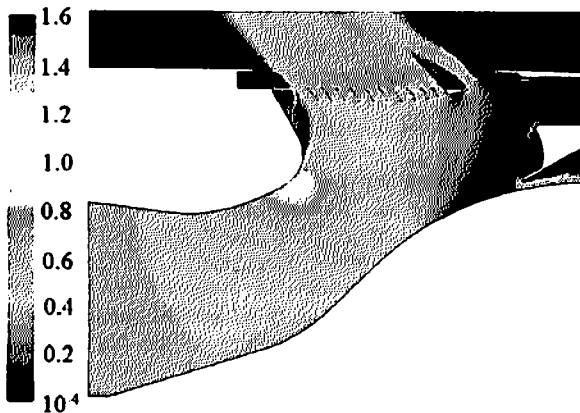


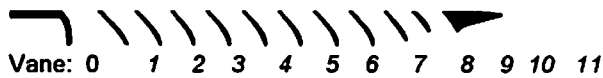
Figure 19. (a) No porous surface on diverter fairing, (b) Effect of porous diverter Mach number contours.

CFD simulations were performed on a two dimensional model using Fluent 5™ in order to understand the aerodynamic performance of the natural blockage thrust reverser, fully deployed. The test cases included three thrust reverser configurations: a base line with cascade vanes, a configuration with a porous diverter fairing and the cascade vanes removed, and a configuration with a reduced number of cascade turning blades. Two types of grids were used: an unstructured non-uniform grid for the whole computational domain (Fig. 17 – Grid 1) and a hybrid, unstructured non-uniform grid with a structured grid inside the boundary layer (Grid 2). In both cases grid independence studies were performed. There was no significant difference between the solutions of those two grid systems (Fig. 18). The CFD predictions for the baseline model were validated against wind tunnel test data collected at Flow Science Ltd, Manchester, UK, by Bombardier Belfast on a 40% scale model of the natural blockage thrust reverser (to be published). Details of the investigations on the natural blockage thrust reverser are given in Refs 62-77.

The Mach number distribution in the natural blockage thrust reverser with and without flow control in the form of a porous diverter is shown in Fig. 19. The passive control device consists

of a porous surface with a plenum chamber: there is no active suction. It is seen that the basic configuration (Fig. 19(a)) has regions of supersonic flow with separation and associated instabilities, whereas the configuration with a porous surface (Fig. 19(b)) has no supersonic flow or flow separation on the diverter fairing. The flow field in the fan duct has been significantly improved by the inclusion of a porous area in the diverter fairing, although there is a small reduction in the reverse thrust.

Typical cascade configurations used to investigate the effect of cascade blades on the performance and weight are shown in Fig. 20. The corresponding Mach number contours for the flow are shown in Fig. 21. For design 1 (Fig. 21(a)), with the thrust reverser deployed, there exists supersonic flow at the diverter fairing. Mach number contours for design 2 (Fig. 21(b)) show that the flow is subsonic. This design produced a 10% reduction in weight and an improvement in the structural performance through reductions in both maximum vane displacement and mid-vane stress levels. However there is a penalty in reverse thrust, which was reduced by 9%. Cost and ease of manufacture will also have to be taken into consideration before any firm conclusions are drawn regarding a final cascade configuration.



(a) Cascade Design 1, Original.



(b) Cascade Design 3, 10% Weight Reduction.

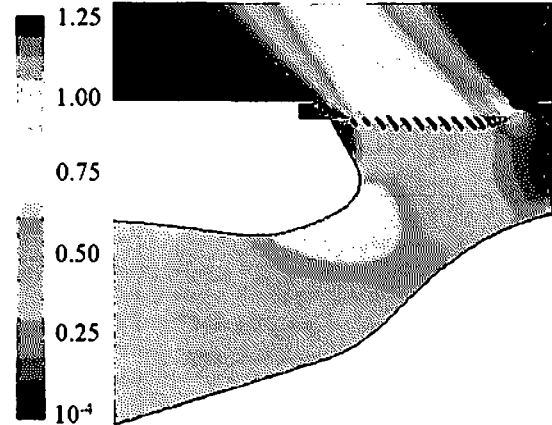
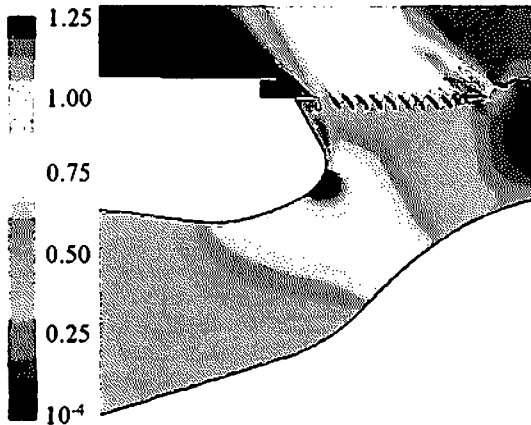


Figure 21. Cascade design for weight reduction. Mach number contours. (a) Design 1, Original, (b) Design 2, 10% Weight reduction.

### 3.2 Natural blockage thrust reverser – cascade-less

Cascade vanes can be costly to manufacture and maintain, and have a weight penalty associated with them. Having no cascade vanes removes these disadvantages and allows the cavity in the transcowl to be closed over. However, the reverse thrust performance is markedly reduced with such a configuration. The inclusion of a slat close to the diverter fairing improves the reverse thrust performance by controlling the flow at the diverter fairing. CFD analyses of the cascade-less configurations, with and without a slat, have been carried out and typical Mach number contours are presented in Fig. 22. These CFD predictions have been validated against wind tunnel test data collected at Flow Science Ltd, Manchester, UK on a 40% scale model. Although the tests were not fully exhaustive the cascade-less configuration gave a reverse thrust performance that was 75% of the configuration with cascade vanes. Consideration of the test results indicate that with careful choice of diverter fairing and transcowl geometry, slat profile and slat position a reverse thrust performance that is 90% of the cascade vanes configuration is achievable.

## 4.0 FIRE ZONE VENTILATION<sup>(78-90)</sup>

The safe and efficient operation of aircraft turbofan engines requires effective ventilation of the nacelle zones. Ventilation of the nacelle is required to avoid the build up of hazardous vapours, which may contribute to the initiation or continuance of an engine fire, and in the event of a fire the ventilation must ensure correct dispersal of the fire-extinguishing agent. In addition, cooling of critical components within nacelle zones is also achieved through the provision of ventilating flows. This may include forced cooling of the engine casing in order to improve specific fuel consumption by maintaining minimum compressor and turbine tip clearances. The

constraints on the design of adequate ventilation systems are legion, including: externally, the position of the engine on the aircraft (wing or aft fuselage mounted); internally, whether the zone to be ventilated is the fan cowl casing or core engine casing, structural design, the locations of major systems (such as the thrust reverser, gear box, oil cooler, fuel system and lubrication system); and operational considerations such as the required number of volume changes per minute and the outside air temperature and Mach number. With such a range of constraints it is not altogether surprising that the system design is finalised after the other major items have been frozen. This can result in over-design of nacelle components, leading to increased weight, part numbers and cost. However, before the certifying authorities approve any new system for operation, it is necessary to demonstrate that it meets the airworthiness requirements, and the certification tests can be fraught with uncertainty because of the general ad hoc nature of the ventilation system design.

Within the last decade, Bombardier and QUB have collaborated on four research projects aimed at elucidating the nature and performance of ventilation systems. These were: fire propagation and heat transfer modelling within the BR710 nacelle for certification purposes<sup>(79)</sup>; performance enhancement of auxiliary air intakes<sup>(60,81)</sup>; aerodynamic performance of pressure relief doors on engine nacelles<sup>(82)</sup>; and fire suppressant dispersion<sup>(83,90)</sup>.

### 4.1 Fire zone modelling<sup>(78,79)</sup>

An attempt was made to model fire propagation and heat transfer in the fan compartment, (fire zone one), of the BR710 nacelle. Full-scale experimental tests are prohibitively expensive, and it is possible, in principle, to gain valuable and instructive insights through the application of computational models. However, fire zones are typically geometrically cluttered environments, and initial attempts to model the fan compartment zone of the BR710 nacelle

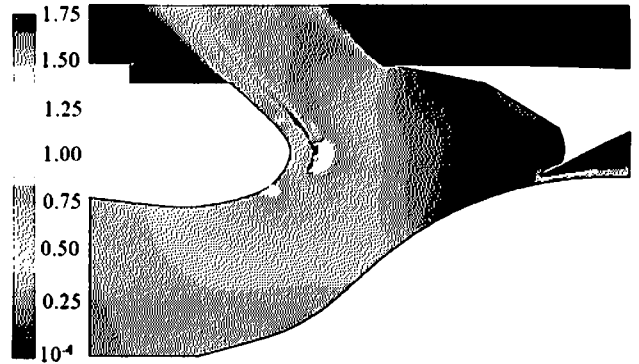
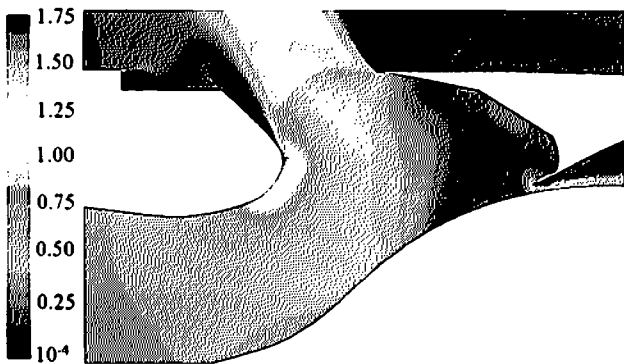


Figure 22. Cascadeless thrust reverser Mach number contours. (a). Without Slat; (b). With Slat.

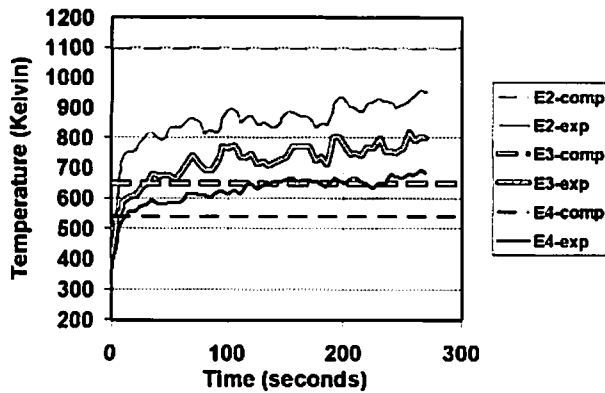
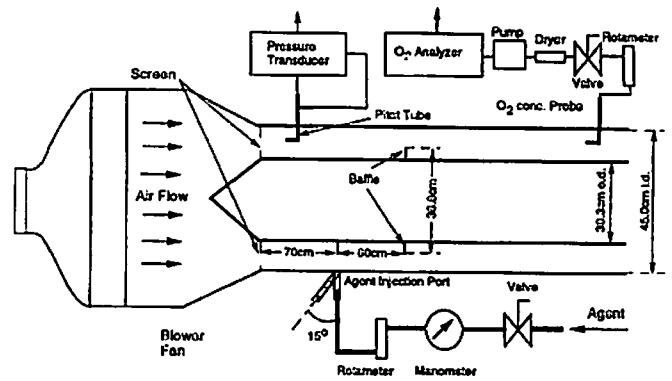


Figure 23. Measured and predicted temperatures inside fire zone.



(a) Tunnel setup.

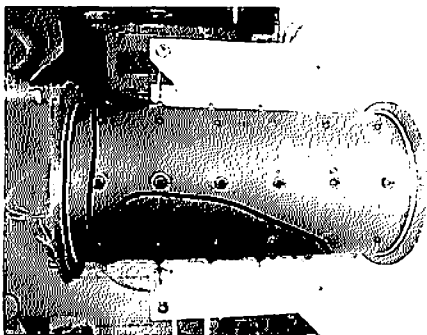


Figure 24. Side view of inner cylinder black line added to show limit of carbon deposits after sustained combustion.

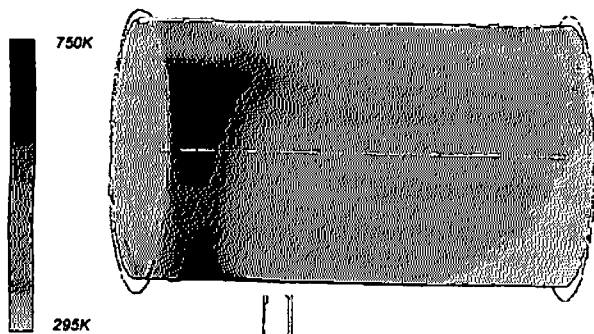
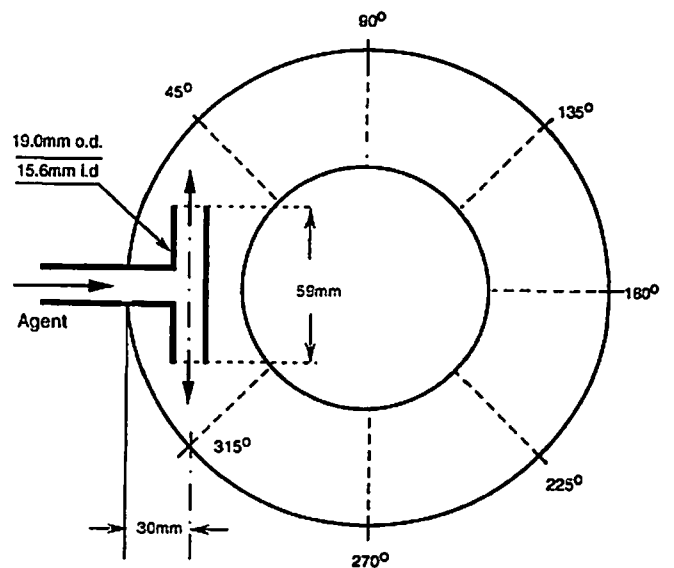


Figure 25. Side view of predicted temperature distribution on a surface midway between the inner and outer walls of the annulus



(b) T injection nozzle. The flow direction is into the plane of the page.

Figure 26. Schematic of the experimental setup<sup>(85)</sup>.

faithfully were abandoned as it was recognised that there was too much uncertainty about achieving a reliable model of the convective flow in the zone, not to mention the difficulties associated with modelling the progress of a combustion process. Instead, the fire zone was modelled as an annular cylinder, approximately 1:5 scale of the fire zone of which it was an idealisation. Forward and aft Y-shaped vents placed at 12 o'clock on the outer surface of the annulus, and a rectangular outlet normal to the axis of the cylinder and placed at 6 o'clock on the outer surface provided ventilation. Both experimental and computational flows, non-combusting and combusting, were investigated.

The fire test simulation was that of a 'ventilated limited flame', i.e. the fuel source enters the zone at a strategic point corresponding to the likelihood of a fuel pipe leak with an ignition point placed directly opposite the point of fuel entry. The only source of oxygen to sustain the flame is that of the ventilation system. Five sets of conditions, typical of take-off, climb and cruise, were investigated. Two fire scenarios were considered, namely, explosive potential and sustained combustion. Fluent 5™ was used for the calculations. Generalised finite rate models were used for the explosive scenario, and the mixture-fraction/probability density function (pdf) formulation for the sustained combustion cases. The tests employed propane as the fuel, rather than kerosene, because it is clean, gaseous at the operating conditions, more easily modelled than kerosene, and yet exhibits similar flammability properties, such as heat of combustion.

The explosive scenario proved to be very difficult to model. Thermal boundary conditions modelling the radiation of heat away from the annulus could not be applied because of computer memory constraints. The explosion was very rapid, and very small time steps were required to capture the first 0.5 seconds, after which the temperature of the outlet gases dropped very rapidly to a steady state that indicated the end of combustion. The response times of the temperature probes used to measure the temperature in the annulus were too long, by an order of magnitude, to capture the transient temperature rise, and consequently, no tie-up between the calculations and the measurements was possible.

The sustained combustion case was more yielding to investigation. Temperature was measured at several locations around the annulus, and a comparison of the measurements and predictions showed similar trends (Fig. 23). Moreover, the deposition of soot on the inside of the experimental annulus was taken as an indication of the regions, within which combustion was concentrated, and therefore also indicative of flow patterns (Fig. 24). Similar patterns were observed in the predictions (Fig. 25). Both experiments and calculations revealed consistent trends, indicating hot-spots in which the air temperature rose to between 800°C and 1,100°C, while the air temperature in the rest of the zone remained in the range 40°C to 100°C. This suggests that whole zone heating is not as prevalent as was initially assumed.

## 4.2 Fire suppressant dispersion

The complex ventilation flow in the fire zone makes it difficult to predict the dispersion of the fire-suppression agent, and hence the performance of the fire-suppression system. At present, the performance of the fire-suppression system is evaluated by ground tests or flight tests. Typically, the injection nozzle type, number, location and orientation and the layout of the delivery lines are modified until the system passes the certification test outlined by the FAA<sup>(83)</sup>. The certification test procedure involves releasing the agent from the bottle, and measuring the agent concentration at twelve different locations inside the nacelle. To pass the test, a minimum agent concentration (6% by volume for Halon 1301) must be observed simultaneously at all twelve probe locations for a minimum of 0.5s. Certification is a time consuming and expensive process, which comes late in the overall design cycle, and so can lead to programme delays and cost overruns.

The current design procedure for the fire-suppression system relies on engineering judgment and empiricism. It has been reasonably successful in the past, mainly due to the effectiveness of Halon 1301, the fire-suppression agent traditionally used in aircraft engine nacelles. However, Halon 1301 has a high ozone-depleting potential, and its production was banned as a result of the 1994 amendment to the 1987 Montreal Protocol<sup>(84)</sup>. Despite significant research effort<sup>(85-87)</sup>, a 'drop-in' replacement for Halon 1301, with acceptable levels of suppression effectiveness, ozone-depleting potential, global warming potential, and toxicity has not yet been found. It seems likely, however, that Halon 1301 will be replaced with a less effective agent, and so it will be important to improve the performance of the fire-suppression systems, to make the most efficient use of the agent. It is envisaged that CFD could provide a better understanding of the agent dispersion, and ultimately deliver a validated engineering tool to aid the design and certification of the fire-suppression system. With the aid of CFD, future fire suppression systems will be lighter, cheaper and safer than today's overly conservative designs.

The dispersion of fire suppression agents in aircraft nacelles has not received a great deal of attention in the literature. Hamins *et al.*<sup>(88)</sup> performed both experiments and simulations of suppressant transport in a smooth annular geometry. They studied the dispersion of N<sub>2</sub>, which was injected into the annular domain through either a T-junction or a round nozzle. In some cases clutter was placed on the inner wall of the duct, in the form of a small transverse rib. Hamins *et al.* only had a limited degree of success with their CFD simulations; in most cases the correct trends were predicted, but the overall correlation with their experimental data was relatively poor. They suggested that deviations were probably due to the use of the k-turbulence model. Lopez *et al.*<sup>(89)</sup> studied the flow of a suppressant in an uncluttered F-18 engine nacelle: they claimed that this was the first attempt to model agent dispersion in a realistic geometry. They obtained a good agreement between their CFD results and earlier experimental results. The oxygen concentration was slightly over-predicted, and this was attributed to the fact that they did not model the fire that was present in the experiments. Later, the same group of workers performed simulations using the VULCAN fire field model and reported that the velocity field was relatively unaltered by the presence of a fire<sup>(90)</sup>.

The aim of the work at Queen's University of Belfast was to use CFD to replicate the experiments of Hamins *et al.*<sup>(88)</sup>, to begin validating the use of CFD for predicting agent dispersion in engine nacelles. The experimental geometry is shown in Fig. 26. The N<sub>2</sub> was injected through either a T-junction (Fig. 26(b)) or a round nozzle. The commercial CFD code Fluent 6™ was used to study three main configurations: T injection nozzle, T injection nozzle with a rib on the inner wall of the duct, and round injection nozzle. The N<sub>2</sub> was injected at a rate of 0.0137kg/s and the tunnel velocity was 3ms<sup>-1</sup>. The species transport model was used in conjunction with the main flow and turbulence equations. Various k-ε and k-ω turbulence models were tested. Unstructured wall-function meshes were used, since the ultimate aim is to simulate the flow inside a cluttered nacelle. To obtain a good correlation with the experimental results, it was essential to use adaptive mesh refinement in the N<sub>2</sub> plume.

As the agent issues from the T injection nozzle, it impinges on the wall of the duct, and spreads in the circumferential direction as it travels downstream (Fig. 27). The volumetric concentration profile for the T injection nozzle case is plotted in Fig. 28. The measurements were taken at various circumferential positions midway between the inner and outer duct walls, 96cm downstream of the injection nozzle. There is a definite asymmetry in the experimental concentration profiles, which could not be explained by Hamins *et al.*<sup>(88)</sup>. For the clean duct (Fig. 28(a)), the correlation between the CFD results and the experimental results is excellent. When the rib was introduced (Fig. 28(b)), the N<sub>2</sub> concentration was lower for 135° < θ < 225°, since the rib slowed the spread of the agent in the circumferential direction. The CFD results were qualitatively

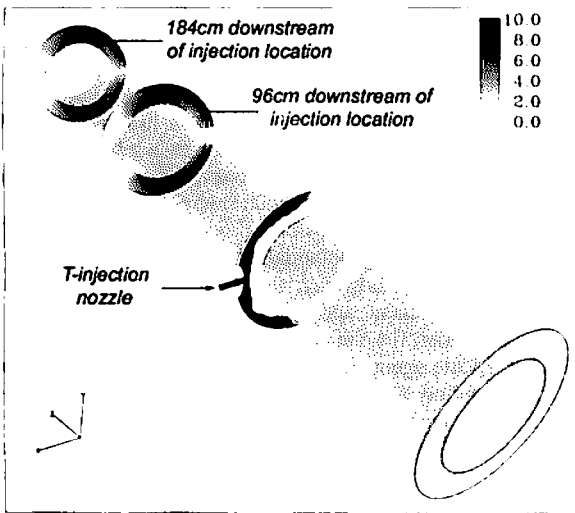


Figure 27. Volumetric concentration of  $N_2$  (%) at various axial planes downstream of the T injection nozzle.

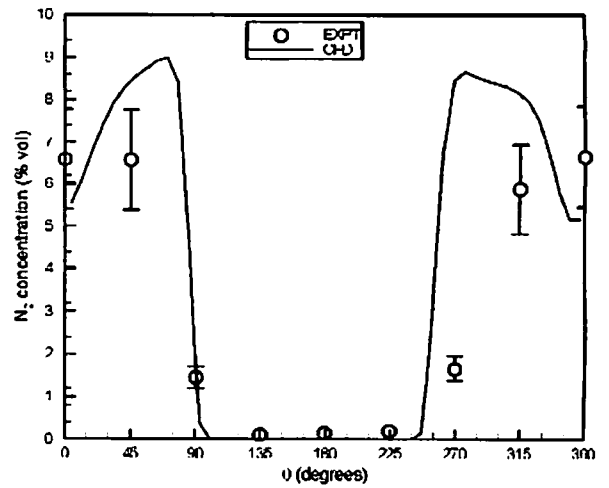
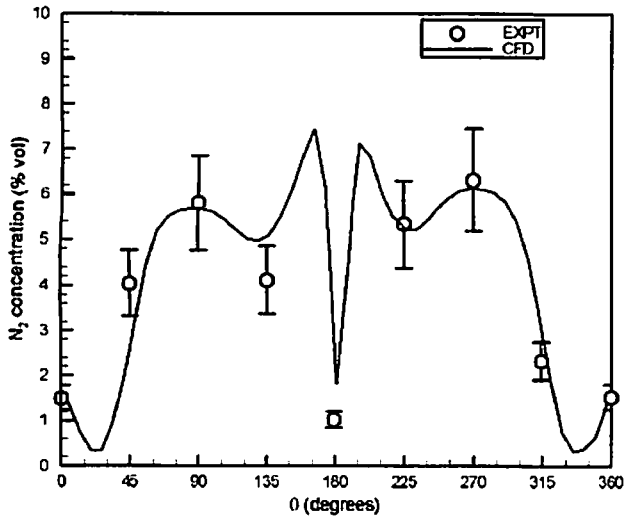
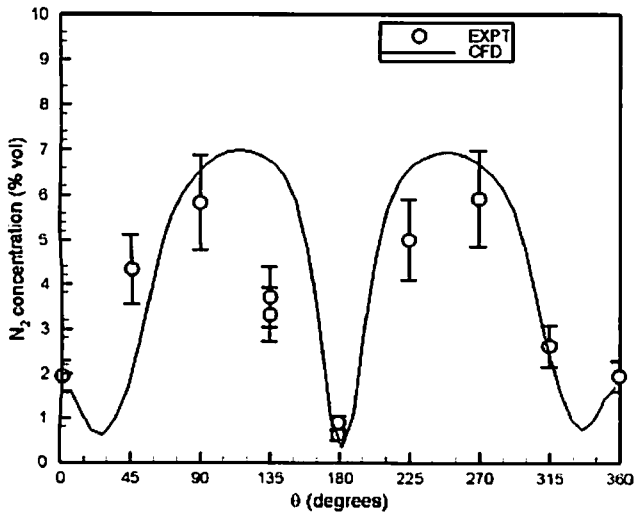


Figure 29.  $N_2$  concentration versus circumferential position, for round injection nozzle case.

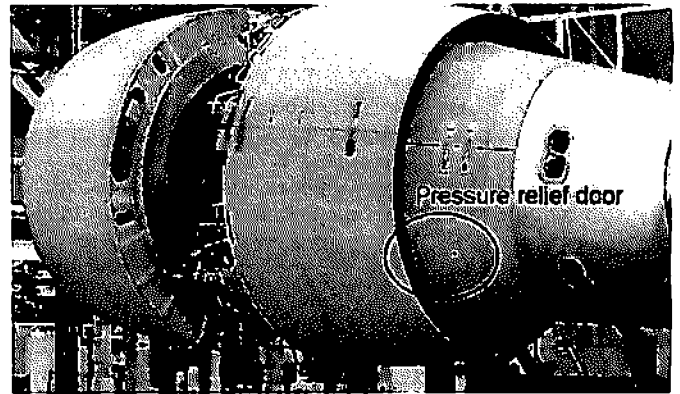


(a). Clean duct.



(b). With a rib on the inner duct wall.

Figure 28.  $N_2$  concentration versus circumferential position for T injection nozzle case.



(a). Location of pressure relief door.



(b). close-up of door.

Figure 30. Typical engine nacelle and pressure relief door.

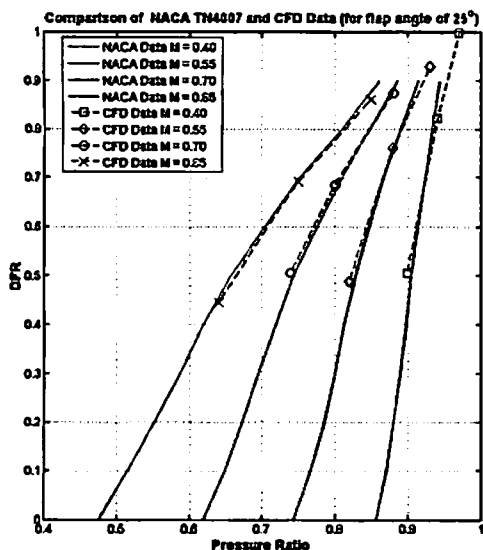


Figure 31. Measured and predicted discharge coefficients as functions of pressure ratio for flap angle = 25°.

correct, but the concentration levels were slightly high for  $135^\circ < \theta < 225^\circ$ . For the round injection nozzle (Fig. 29), there is a significant change in the concentration profile compared to the T injection nozzle. The concentration levels are extremely low for  $90^\circ < \theta < 270^\circ$ , and very high elsewhere. The agent dispersion is much better for the T nozzle. The CFD results for the round nozzle show a fair correlation with the experimental values. To conclude, CFD can model the dispersion of a model fire suppressant with a reasonable degree of accuracy, provided adaptive grid refinement is used in the agent plume region. Further validation is underway to study the effect of introducing more clutter into the domain.

### 4.3 Pressure relief doors

An important set of auxiliary engine outlets is related to pressure relief in the case of duct burst in the nacelle compartment. Typically pressure relief doors (PRDs) are rectangular in geometry with a door hinged on either the forward or side edge (Fig. 30). In the event of a duct burst, the pressure that builds within the compartment would compromise the nacelle structure were it not for the pressure relief doors that are installed to regulate the pressure to an acceptable value.

The designer of PRD installations must have reliable data on force and discharge characteristics. Very little research has been done on this subject, especially in recent years. Current designs have been based on experimental data presented in NACA TN400791 regarding the discharge characteristics of flapped, curved duct outlets in transonic flows. Consequently a conservative approach to analysis has been adopted by the aerospace industry. More detailed information is now required to achieve a design that satisfies customers and certifying authorities but is not overly conservative. It is proposed to achieve this through systematic computational investigations, supported by experimental studies. The database should help directly the designer to improve the overall performance, both aerodynamic and structural, of the device.

The commercial CFD package, Fluent 6™, was used to model the experimental work described in NACA TN4007. The computational domain was a rectangular duct 25.4mm wide by 46.7mm long, which turned the exhaust flow through 90° about a radius of curvature of 50.8mm into the stream-wise direction. The upstream edge of the orifice was extended 9.5mm so that the orifice length

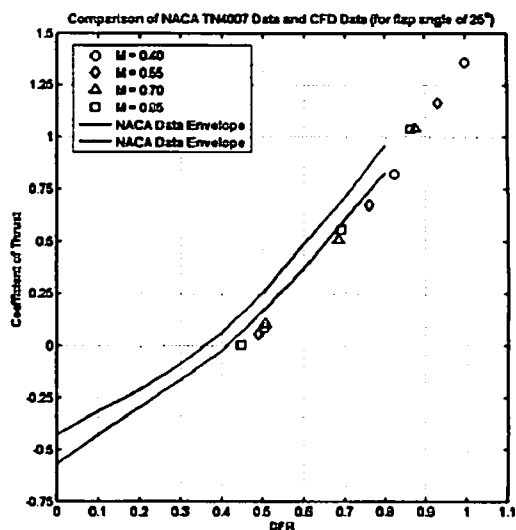


Figure 32. Measured and predicted thrust coefficients as functions of discharge coefficient for flap angle = 25°.

was 37.8mm. A flat, rectangular flap 25.4mm wide by 25.4mm long was attached to the upstream edge of the duct orifice. The orifice leading edge was placed 203mm downstream of the inflow boundary. The computational domain being symmetric, only one half, measuring 432mm long by 79.4mm wide by 114.3mm tall was modelled.

Flap angles of 15° to 45°, in 5° increments, were studied. The free stream Mach number was varied from 0.4 to 0.85 in increments of 0.05. As a result, the ratio of boundary-layer thickness to orifice length varied between 0.095 and 0.110. The pressure ratio was varied between 0.64 and 0.97 in order to obtain the range of discharge flow ratio coefficients (DFR) required. The realisable  $k-\epsilon$  turbulence model was used because it is of known accuracy when dealing with flows involving jets, separations and secondary flows. A mesh dependence study was performed to ensure that converged solutions were mesh independent.

Typical results are shown in Figs 31 and 32. Generally good agreement was obtained between measurement and prediction of integral quantities such as DFR and thrust coefficient. Predictions under-estimated the discharge by between 5% and 20%, depending on pressure ratio; the thrust coefficient was slightly over-predicted.

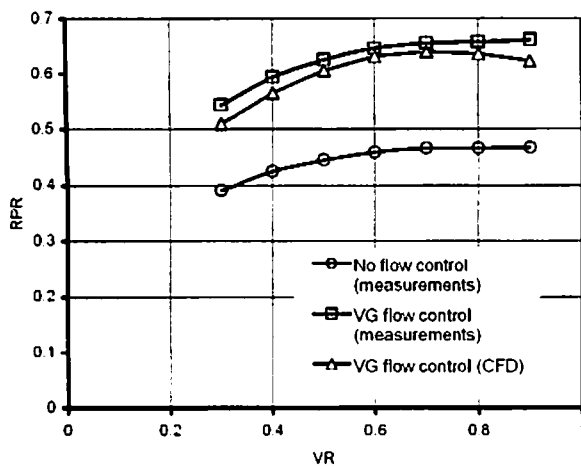
Calculations were performed for a wider range of flap angles than was considered in the experiments, and it was shown that the DFR increases with flap angle up to an optimum value, after which increasing the flap angle decreases the DFR. The value of optimum angle falls with increasing pressure ratio, but is insensitive to free stream Mach number. These effects may be explained, in part, by the strength and orientation of the vortex system generated by the inclined flap, which sets a boundary condition on the flow emerging from the exhaust duct.

It was shown that the angle for which the hinge moment on the flap was zero lay in the range of 10 to 15 degrees for all cases. A freely hinged, weightless flap would, therefore, achieve a trimmed balance in that range of angles. Increasing Mach number decreases this angle, while increasing pressure ratio increases it.

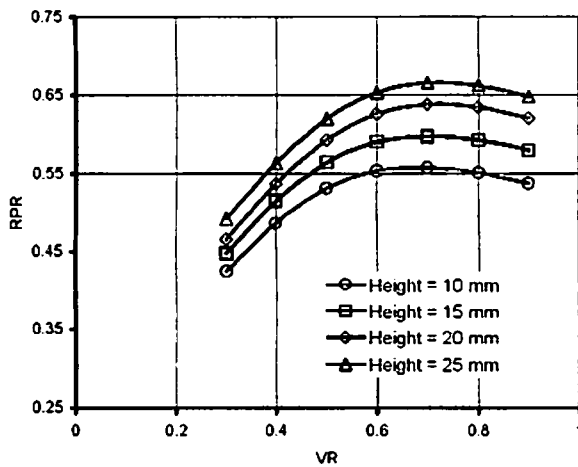
### 4.4 Auxillary air intakes

Auxiliary air intakes perform a variety of functions on aircraft, from cabin air supply, to engine component cooling and fire zone purging. The intakes come in a number of forms, including pitot designs,

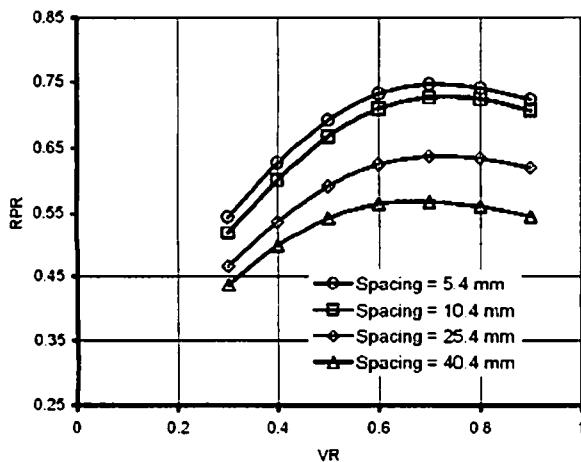




(a) Effect of flow control, measured and predicted.



(b) Predicted effect of spacing of vortex generators.



(c) Predicted effect of height of vortex generator.

Figure 33. RAM pressure recovery vs velocity ratio.

fared surface mounted blisters and flush intakes. Intake performance is characterised by the amount of air that can be swallowed for a given pressure drop (Fig. 33). Flush intakes are generally either parallel walled or of the NACA contoured converging wall design. The former design is simpler, and less expensive to manufacture and maintain, but has inferior performance, so that a larger, heavier intake, with a greater drag penalty is necessary to match the capacity of the equivalent NACA intake. The volume flow rate versus ram pressure recovery (RPR) characteristic of the flush intake is a function of the ratio of the boundary layer thickness ( $\delta$ ) to the intake scale, usually represented by depth ( $d$ ). The performance of the intake is degraded as this ratio increases.

Vortex generators (VGs) have been used for decades to improve the high lift capability of aircraft wings. Vane type generators are the most common form, but all have much the same mode of operation: a longitudinal vortex is generated with a diameter of the same order of magnitude as the boundary layer thickness. It is embedded within the turbulent boundary layer so that it draws high momentum flow from the external mainstream down into the lower third of the boundary layer. The boundary layer is thinned in the downwash region, and thickened in the upwash region. VGs are often used in arrays: co-rotating (all the VGs aligned the same way) and counter-rotating (VGs alternately at positive and negative incidence) arrays are possible. In counter-rotating arrays, the region of downwash between VGs is referred to as common-flow-down, while the region of upwash between VGs is referred to as common-flow-up. It is hypothesised that a pair of vortex generators placed upstream of a parallel walled intake, such that the intake lies in the common-flow-down region should reduce the local value of  $\delta/d$  and improve the intake performance.

Experiments were conducted in a closed loop wind tunnel with a test section 575mm  $\times$  375mm. An idealised model of an auxiliary intake was mounted in a flat plate, 870mm downstream of the plate leading edge. The intake had a ramp angle of  $10^\circ$ , a width to depth ratio of 4 and a cross sectional area of 6450.16mm<sup>2</sup>. A plenum chamber 405mm  $\times$  265mm  $\times$  550mm was placed beneath the intake and a flow meter and vacuum pump placed downstream of it. The test speed was 45ms<sup>-1</sup>, and at the intake  $Re_\theta = 6,000$  and  $\delta/d = 1.5$ . There was no external stream-wise pressure gradient. A pair of vortex generators, height 20mm, chord 40mm, apex separation 50.8mm, angle-of-attack  $22^\circ$ , in common-flow-down configuration (i.e. the region between the VGs is common-flow-down) was placed in a turbulent boundary layer of  $\delta = 10$ mm, 400mm upstream of the intake. The total pressure inside the intake was measured using a pitot rake of five probes, which could be traversed normal to the intake wall and laterally. Single wire hot wire anemometry was used to measure the boundary layer in the free stream 150mm upstream.

The computational fluid dynamics package Fluent 6<sup>TM</sup> was used to test more configurations. The domain measured 1,210mm  $\times$  1,050mm  $\times$  500mm and included the test plate and intake, with the intake placed 82mm downstream of the inflow boundary so that experimental data could be used as the inflow boundary condition. A fully block structured mesh of 350,000 cells was created. The software was run in its implicit segregated mode, with several versions of the  $k-\omega$  turbulence model tested.

Typical results are shown in Figs 33 to 35. The application of the vortex generators typically gave ram pressure recovery improvements of between 35% and 40%. Although ingestion of the vortex pair must be avoided, this does not appear to be a problem as the vortices naturally migrate away from the centreline of the intake. The treatment gives the intakes the potential for a peak performance similar to that of the more complex NACA intake. However, the vortices generated by the NACA intake are ingested at high flow rates and the NACA intake's performance drops markedly. Hence, the treated parallel walled intake performs better over a wider range of flow conditions. Designers/manufacturers may be able to use either smaller examples of the treated intake or smaller numbers of them. This would have benefits for aircraft weight, part count and maintenance.

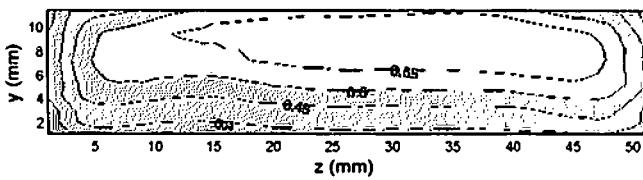


Figure 34(a). VR = 0.5.

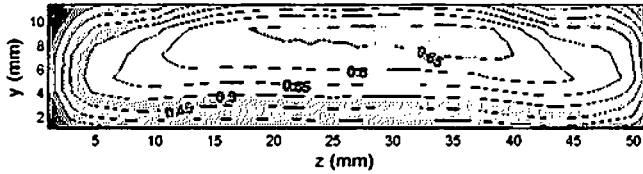


Figure 34(b). VR = 0.7.

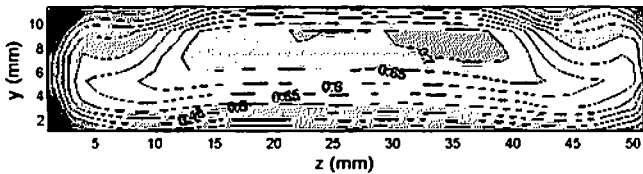


Figure 34(c). VR = 0.9.

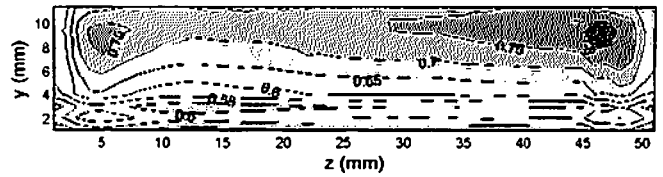


Figure 35(a). VR = 0.5.

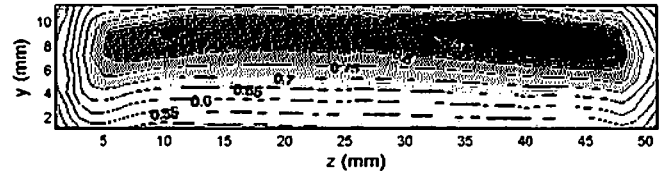


Figure 35(b). VR = 0.7.

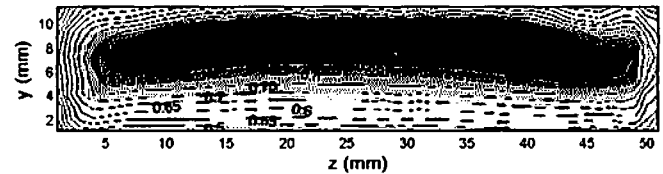


Figure 35(c). VR = 0.9.

## 5.0 NACELLE, PYLON AND WING AERODYNAMIC INTEGRATION<sup>(92-102)</sup>

With today's ever increasing demand for air travel, the environmental impact of aircraft is becoming a major concern. As well as the obvious problem of noise pollution near airports, there is also the issue of CO<sub>2</sub> emissions. As previously stated, ACARE have targeted a 50% reduction in aircraft CO<sub>2</sub> emissions by the year 2020<sup>(92)</sup>. A way of achieving these ambitions targets is to minimise drag for a given lift. In particular when a nacelle and pylon are installed onto an aircraft there is an increase in the aircraft total drag. A part of this extra drag can be reduced through better analysis of the complex interactions between aircraft components. With modern nacelle designs the use of laminar flow technology can also have a significant saving of aircraft fuel consumption. This was demonstrated in flights tests carried out by Rolls-Royce, MTU and DLR<sup>(93)</sup> where net sfc was decreased by 2%.

There has been a number of investigations carried out in the past on the aerodynamic interactions of the nacelle, pylon and wing. These can be broken down into four areas: interference effects of the nacelle, pylon and wing; the effect of different nacelle position; the effect of high bypass ratio (BPR) and ultra high BPR nacelles; and the ability of CFD to predict the interference effects.

Once the nacelle and pylon are installed onto an aircraft wing, the aerodynamic performance of the wing changes significantly. There is an increase in total drag, a loss of total lift<sup>(94)</sup> and the shock wave position on the upper surface of the wing changes. Also affected is the wing spanwise loading, which will in turn cause an change in induced drag. There is no agreement as to the source of these degradations, with some authors concluding the pylon shape is to blame<sup>(95)</sup> and others concluding the channel effect of the nacelle, pylon and wing is to blame<sup>(96)</sup>.

Another area of investigation is the effect different nacelle and pylon locations have on the aerodynamic performance of the aircraft.

Godard *et al*<sup>(97)</sup> studied the effect of changing the position of the nacelle both vertically and horizontally. The most sensitive change in position of the nacelle was found to be the horizontal position. The best result for minimum drag was found to be furthest upstream from the wing. The change in vertical distance had much less effect on drag. The reason for this was that when the nacelle was closest to the wing the area between the top of the nacelle, the pylon and the bottom of the wing was contracting. This resulted in an acceleration of the local flow and a shock wave. This caused the drag of the aircraft to increase and the lift to decrease. When the nacelle was at the most upstream position, the area in this region was greater, which reduced the local velocity and the adverse interference effects. However, the further the nacelle is away from the wing the greater the structural weight penalty is.

The effect of larger BPR nacelles has received the most attention in previous projects. This is because larger BPR engines have better fuel efficiency<sup>(98)</sup>, but, of course, larger nacelle diameters. The largest BPR engine today is on the Boeing 777, which has an engine BPR of nine. These large diameter nacelles lead to greater interference effects<sup>(99)</sup>. However it is also reported that the higher BPR engines could have the same impact on aircraft drag as smaller engines 100.

The CFD methods used to simulate the nacelle, pylon and wing interference effects have been developed over the past 15 years. The earlier calculations were performed using inviscid Euler codes<sup>(101)</sup>. The next step was the used of Euler codes with viscous corrections<sup>(102)</sup>. In recent years Reynolds Averaged Navier Stokes (RANS) calculations have been performed<sup>(103)</sup>. The capability and computational resource required of each in predicting the interference effect is different. Euler calculations can predict the change in lift when the nacelle and pylon are installed and is computationally inexpensive. However the accuracy of the lift values is inadequate and drag implications cannot be predicted. Euler calculations with viscous effects can predict the lift more accurately and also the changes in lift.

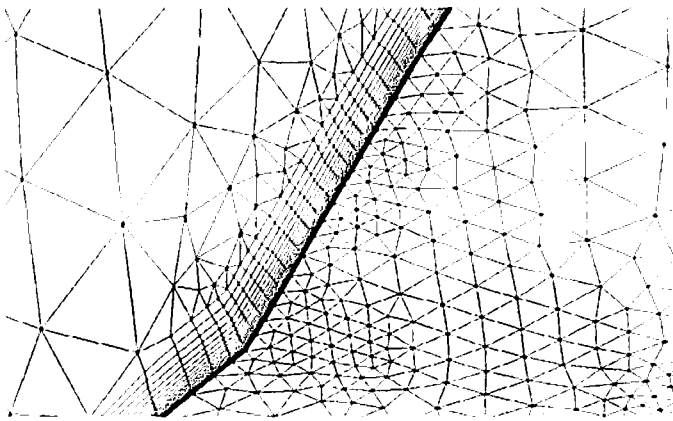


Figure 36. Prismatic layers from fuselage surface.

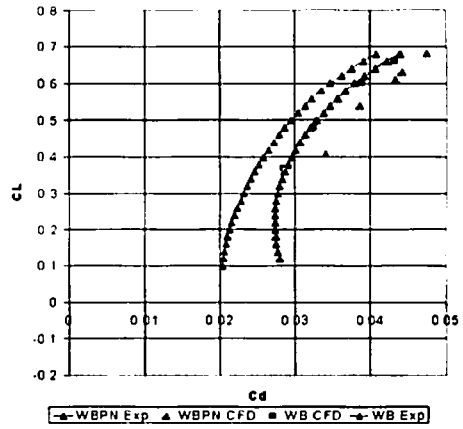


Figure 37. Predicted and experimental lift coefficient vs drag coefficient.



Figure 38. Compression pylon shape.

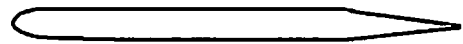


Figure 39. Conventional pylon shape (DLR F6).

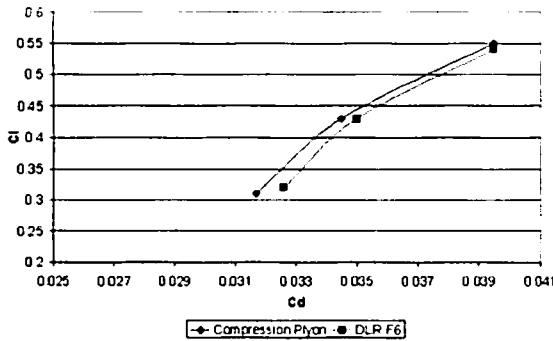


Figure 40. Predicted Lift vs drag of baseline case to compression pylon case.

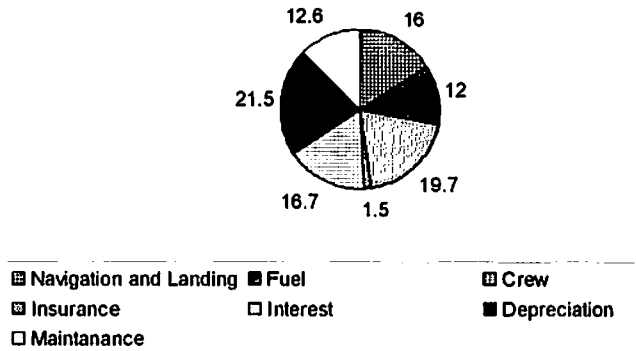


Figure 41. Typical percentage DOC distribution for a commercial aircraft.

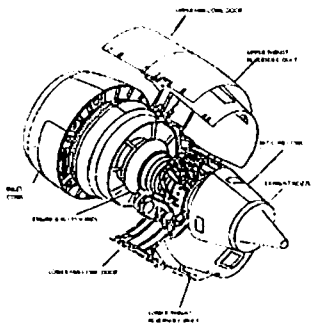
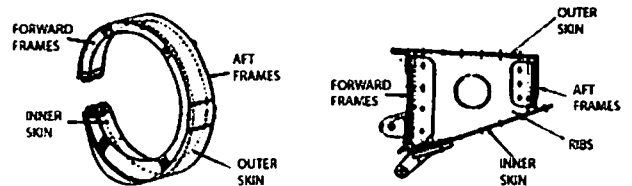


Figure 42. Illustration of typical nacelle design.



	Before	After	Percentage Reduction
Number of Parts	110	86	22
No. of Fasteners	1090	916	16
Assembly time (Hrs)	116	96	17
Weight (lbs)	86	71	17
Recurring manufacturing Cost		500	

Figure 43. Results from DFMA implementation on the redesign of a nacelle torque box.

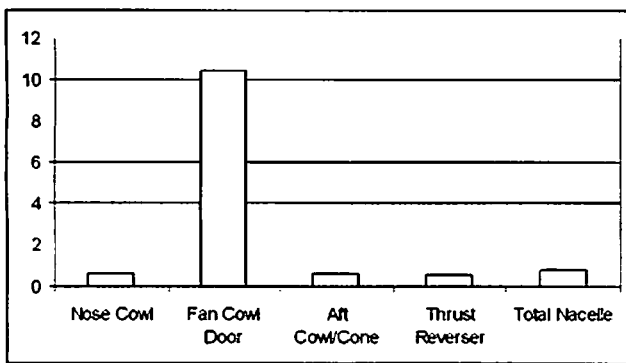


Figure 44. Part counts of nacelle B normalised with respect to nacelle A.

However the drag implications cannot be predicted and the computational cost is three times that of the basic Euler calculations<sup>(34)</sup>. RANS calculations can predict the lift accurately and the change in lift. In addition, the drag implications can be predicted, which means a full investigation can be performed. However the computational cost can be as much as hundred times greater than the basic Euler calculations<sup>(34)</sup>.

This research was completed using an unstructured mesh and solver. The computational fluid dynamics package Fluent 6™ was used and the mesh was generated using ICEMCFD™. The reason for choosing unstructured meshing techniques was the relative automation of mesh generation. To meet the mesh requirements for an accurate simulation using unstructured meshes is difficult, especially in the near wall regions. A solution to this problem is to create a hybrid mesh, which allows for sufficient grid resolution in the near wall region. To create a hybrid mesh using ICEMCFD, prismatic layers were grown from a surface mesh. The first cell height was set to 0.003mm and 30 prismatic layers were grown at a growth rate 1.2 (Fig. 36), resulting in a mesh  $y^+$  of approximately 1.

To validate the computational methodology the flow over a variant of the DLR-F6 was simulated. This configuration was subjected to many wind-tunnel experiments in the 1990s. The CFD results obtained in this work were compared to published experimental data on the DLR-F6. The predicted and experimental drag polar can be seen in Fig. 37 for the wing body configuration and the wing body nacelle pylon configuration. From this figure it can be seen the total drag for both cases is over predicted for every design point, by approximately 12%. However, with closer analysis of the results the predicted drag rise due to the installation of the nacelle and pylon was predicted to within 1% of the experimental result. Therefore using these computational methods one could compare different configurations and accurately predict the drag change of each within sensible limits. Using this validated technique a new pylon design was investigated to determine the influence of the pylon. The conventional pylon shape was redesigned to a compression pylon shape (Figs 38 and 39). The new design had an impact on the drag of the aircraft. Studying the result in Fig. 40 it is clear the drag has reduced for each design point by as much as five drag counts.

## 6.0 AERODYNAMIC DESIGN TRADE-OFF MODEL FOR MANUFACTURING AND COST<sup>(104-111)</sup>

In recent years, customer needs in the commercial Aerospace sector have been governed by reduced lead-time and cost, while also looking for enhanced aircraft performance and safety measures<sup>(104,105)</sup>.

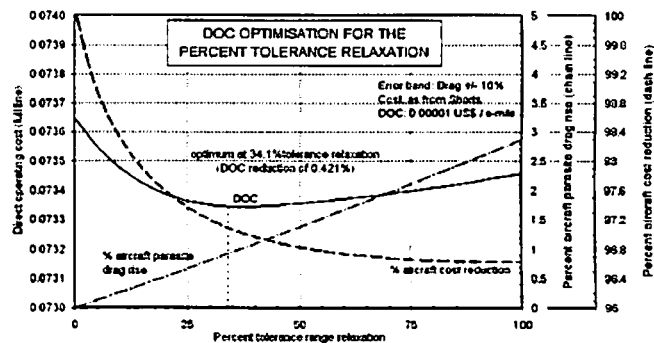


Figure 45. Trade off between aerodynamic and manufacturing tolerances for cost.

A typical Direct Operating Cost (DOC) breakdown of the Airbus A320 class of aircraft (150 passengers and 2,800 nautical mile range, Fig. 41) shows that the aircraft cost contribution to DOC is more than four times that of the fuel contribution. This is even more extreme for smaller aircraft with a lower payload range. It is understood in the aerospace industry that any reduction in DOC requires not only a better understanding of aerospace disciplines but also an understanding of the sensitivity of each discipline to the other. QUB in partnership with Bombardier Belfast took the initiative in this area of research, in 1996; through the EPSRC IMI managed programme (SOAMATAS), where a novel concept of trade-off study between costs associated with two design drivers, aerodynamics (fuel) and manufacturing were conducted. The findings from this programme led to the just completed EPSRC funded programme DEMARDOC where the concept was extended to trade-off studies between wider ranges of design drivers; including aerodynamics, structural configuration, manufacturing and assembly. Details of these investigations are given in references<sup>(105-111)</sup>.

A particular component of an aircraft was chosen for a detailed programme of research. This was the nose cowl of two generic nacelles described in the next Section. The road map for DOC estimation consisted of the development of a rapid cost model based on the baseline design and validated against the later design. Cost reduction measures for the structural part fabrication and their assembly was investigated. The savings were extrapolated for the aircraft and corresponding DOC savings for the mission profile were estimated.

### 6.1 Development of an optimised design to reduce nacelle manufacturing cost

The major objectives involved: (a) development of an accurate cost model and (b) development of a methodology for evaluation of the cost benefits of design for manufacturing and assembly (DFMA) in addition to tradeoffs between aerodynamics and manufacturing.

A rapid cost-modelling methodology was developed that was specifically aimed at catering for the industrial needs of DFMA during the conceptual design phase. The rapid cost model was based on parametric methods taking into consideration the effects of engineering decisions on cost and the link between design statistics and manufacturing cost. In the process of cost modelling, methodologies were also established for cost data collection, definition and accounting. From a baseline cost, the method demonstrated a fast and relatively accurate prediction for the later design.

The task concentrated on cost modelling of the structural elements of generic nacelles. The task was conducted in two steps. First, a detailed cost model was developed for the 'Nose Cowl' and then the model was extended to the complete nacelle. The generic nacelle is

shown in Fig. 33. Two nacelles, A and B, were considered in the modelling. Nacelle A was an existing product and that was taken as the baseline design, whereas nacelle B was a newer design with higher specification standards and 50% more thrust than the baseline turbofan of that family of nacelles. The aerodynamic mould-lines of both the nacelles were similar, but their structural design philosophy, hence the sub-assembly (tooling concept) differed. The manufacturing cost of the finished product consisted of: cost of material (raw and finished product); cost of parts manufacture; cost of parts assembly to finish the product; cost of support (to ensure quality); amortisation of non-recurring costs; and additional miscellaneous cost (contingencies, etc.). (The actual cost data is classified 'commercial in confidence', so relative results are shown.)

Structural components and Engine Built Unit (EBU), e.g. anti-icing units and valves, were considered in the cost modelling, but the EBU costs were separated and are not included in the presented research. Eleven cost drivers in two groups were identified for the analysis. Group 1 related to in-house data within the organisation and consisted of eight cost drivers, namely: size, material, geometry, technical specification, structural design concept, manufacturing philosophy, functionality, man-hour rates (overheads etc.). Group 2 cost drivers consisted of role (e.g. military or commercial), scope and condition of supply, and programme schedule. As they were not concerned with the in-house capability issues they were not considered in this project.

The methodology applied was based on the factors/indices of nacelle B, in relation to the baseline cost of nacelle A, and the associated cost drivers mentioned earlier. The total manufacturing cost of the nacelle was the sum of the individual costs of each of the four nacelle components, as given below for the nose cowl cost CNC, being the sum of the following six items:

$$C_{NC} = \sum_i^6 C'_i = C'_{Mat} + C'_{Fab} + C'_{Asm} + C'_{Sup} + C'_{Amr} + C'_{Misc} \dots (4)$$

Where subscript 'Mat' stands for Material, 'Fab' for Fabrication, 'Asm' for Assembly, 'Sup' for Support, 'Amr' for Amortisation and 'Misc' for Miscellaneous Cost.

Methodologies were developed for each of the six cost components. For example, nose cowl manufacturing cost  $C'_{Mat}$  consisted of two items: parts fabrication and parts assembly to finish. Man-hours required for the fabrication of each part and assembly were a combination of operations; machining, forming, fitting and mounting into jigs. Manufacturing cost was expressed as:

Manufacturing cost = rates × man-hours × learning curve factor × size factor × manif. philosophy.

$$\text{or } C'_{Mat} = C'_{Fab} + C'_{Asm} = [(K_{nr})^{0.15} \sum_1^n [\sum_1^n F_1 F_2 \dots F_n] \times (\text{man hour} \times \text{rates} \times \text{learning factor})]_{Fab} + [(K_{nr})^{0.25} \sum_1^n [\sum_1^n F_1] \times (\text{man hour} \times \text{rates} \times \text{learning factor})]_{Asm} \dots (5)$$

This analysis led to a simple tool for the calculation of nacelle B nose cowl cost, as given by:

$$C_{NC,B} = 0.8306 C'_{Mat,NacA} + 1.0878 C'_{Fab,NacA} + 0.759 C'_{Asm,NacA} + 0.05 \times (0.828 C'_{Mat,NacA} + 1.0878 C'_{Fab,NacA} + 0.759 C'_{Asm,NacA}) \dots (6)$$

Analysis of industrial cost data showed that the nose cowl A cost fractions were as follows:

$$C'_{Mat,NacA} / C_{NoseCowl,A} = 0.408, \quad C'_{Fab,NacA} / C_{NoseCowl,A} = 0.349 \\ C'_{Asm,NacA} / C_{NoseCowl,A} = 0.149 \dots (7)$$

Hence the relative cost of nacelle B was expressed as:

$$C_{NoseCowl,B} / C_{NoseCowl,A} = 0.92. \dots (8)$$

Analysis of components such as the fan cowl, thrust reverser and tail cone followed the same procedure as the nose cowl. In developing

this methodology several aspects of manufacturing and assembly were taken into consideration. These include, part count for the assembly, man-hours involved in fabrication and assembly, rework/concessions and quality of the surface finish as typified in Figs 43 and 44. The analysis of certain components such as that shown in Fig. 43 was for re-design change only, where the material type and manufacturing process were not affected. In that case, the frames were manufactured in three sections and joined with splices and rib clip attachments. These were re-designed into one-piece frames that did not require the use of the clips. The results of the approach adopted on Nacelle B (higher specifications and 50% increase in thrust) although, led to an increase in part count for the door by a factor of ten (Fig. 44) resulted in an overall part count reduction of 24% compared to Nacelle A. The increase in structural requirements from the much higher thrust is highlighted by the fact that fastener count actually increased, e.g. by 8% on the nose cowl in order to provide the required stiffness. However, there was a saving of 12% in assembly costs due to the reduction in part count, and the increased number of complex components, which were not manufactured in-house, influenced the material cost increase of 16%. The total reduction in cost was found to be 2% per kilo of structure and therefore the evaluation methodology has been applied to show that DFMA has been able to improve the manufacturability of the design to maintain, and even reduce cost slightly, regardless of a 50% increase in technical design specifications.

## 6.2 Prediction of aerodynamic performance and cost arising from surface tolerance

The prediction of aerodynamic performance arising out of surface tolerances involved two tasks: (a) trade-off studies between aerodynamics and manufacturing to optimise allocation of the tolerances and (b) prediction of performance and DOC.

Aircraft surface smoothness requirements were aerodynamically driven with tighter manufacturing tolerance to minimise drag, where the tighter the tolerance, the higher is the assembly cost in the process of manufacture. A typical DOC distribution shows that fuel cost is only a fraction of manufacturing cost (Fig. 41). A trade-off study between fuel cost and manufacturing cost was performed on an isolated nacelle and the analysis extended to a complete aircraft. Manufacturing tolerance relaxation at eleven key manufacturing features on the surface assembly of an isolated nacelle was studied without unduly penalising parasite drag, using the cost model developed. The drag estimation was based on ESDU data corrected for pressure gradients determined by CFD and experimental studies. The drag data and aircraft operation were used in evaluating the fuel cost. A large amount of manufacturing cost data were obtained from Bombardier Belfast and were analysed in detail for the effect of manufacturing tolerances on cost. Fig. 45 shows DOC and drag variation with surface tolerance relaxation.

The direct operating cost of aircraft was estimated using Association of European Airlines (1989) ground rules. The payload-range for the mission profile was kept constant throughout the aircraft performance analysis.

With conservative estimation, given below is the typical aircraft cost reduction through such a DFMA approach to tolerance allocation, with fuel price taken at US\$0.75 per gallon. The study resulted in approximately 1.28% DOC saving for a 2% saving in aircraft cost involving no drag rise, and additionally, approximately 0.42% DOC saving for a further 1% saving in aircraft cost for tolerance relaxation that did involve drag rise. The total of 1.7% DOC savings translates into savings of \$530 per sortie for the Airbus 320 class of aircraft. With a typical annual utilisation of 500 sorties that totals to \$265K per aircraft. For smaller aircraft the percentage savings could be higher.

## 7.0 CONCLUSIONS

The School of Mechanical and Aerospace Engineering at the QUB and Bombardier have, in recent years, been conducting research into some of the key aerodynamic safety technologies for the next generation of aircraft engine nacelles. Investigations have been performed into anti-icing technology, efficient thrust reversal, engine fire zone safety, noise attenuation and trade off between aerodynamic performance and manufacturing cost.

Studies on the usefulness of the empirical relations developed for hot-air jet impingement on a flat surface for a highly curved two-dimensional surface showed that the flat-plate empirical relations are inadequate for predicting heat transfer on curved surfaces. Extensive experimental work was performed on a piccolo type of anti-icing system. The results led to a unique correlation between average Nusselt number and Reynolds number for such a system. The correlation is independent of the diameter, number and the distance between the holes and the impinging surface provided these are within the known optimal range, depending mainly on mass flow per unit area and weakly on jet spacing. The effect of normal vibration on heat transfer is negligible and normal vibration of an engine is not a key design parameter of an aircraft anti-icing system. When compared with a steady jet piccolo system a pulse jet anti-icing system could produce an enhancement in heat transfer of 10-20% or reduce the bleed air requirements by 10-20%.

CFD analysis in conjunction with Finite Element Analysis was performed on the Natural Blockage Thrust reverser. The results showed that the quality of the flow field in the fan duct was significantly improved and the flow instabilities eliminated, with the introduction of a porous fairing in the duct. A new cascade design with reduced number of blades eliminated the shock waves, produced a 10% reduction in weight and an improvement in the structural performance in both maximum vane displacement and mid-vane stress levels. However, there is a penalty of thrust reversal, which was reduced by 9%. Cost and ease of manufacture will also have to be taken into consideration before any firm conclusions are drawn regarding the final cascade configuration. A cascade-less configuration gave a reverse thrust performance that is 75% of the cascade configuration. Consideration of the test results indicate that with careful choice of diverter fairing and transcowling geometry, slat profile and slat position, a reverse thrust performance that is 90% of the cascade vanes configuration is achievable.

An attempt was made to model fire propagation and heat transfer in the fan compartment (fire zone one) of the BR710 nacelle. Both experiments and calculations revealed consistent trends, indicating hot-spots in which the air temperature rose to between 800°C and 1,100°C, while the air temperature in the rest of the zone remained in the range 40°C to 100°C. Whole zone heating was not as prevalent as was initially assumed.

Simulations were performed to begin validating the use of CFD for predicting the dispersion of a fire suppressant inside the fire zone of an engine nacelle. Accurate results were obtained for a model fire suppressant dispersing in an idealised nacelle, provided adaptive mesh refinement was used in the agent plume region. It was found that using a T injection nozzle, rather than a circular nozzle, improved the dispersion of the agent. The introduction of clutter hinders the dispersion of the agent, and further studies are underway to investigate the flow in a more realistic, cluttered geometry.

Flap type pressure relief doors with flap angles of 15° to 45°, in 5° increments and in the Mach number range 0.4 to 0.85 were studied. Generally good agreement was obtained between measurement and prediction of integral quantities such as DFR and thrust coefficient. Predictions under estimated discharge by between 5% and 20%, depending on pressure ratio; the thrust coefficient was slightly over-predicted. A freely hinged, weightless flap would achieve a trimmed balance in the range of angles considered. Increasing Mach number decreases this angle, while increasing pressure ratio increases it.

An auxiliary parallel wall air intake with a pair of vortex generators placed upstream was studied with a view to enhance the intake performance. The application of the vortex generators typically gave ram pressure recovery improvements of between 35% and 40%. The treatment gives the intakes the potential for a peak performance similar to that of the more complex NACA intake but the treated parallel walled intake performs better over a wider range of flow conditions. Designers/manufacturers may be able to use either smaller examples of the treated intake or smaller numbers of them. This would have benefits for aircraft weight, part count and maintenance.

Validated CFD analysis showed that the drag rise due to the installation of the nacelle and pylon on a wing can be predicted to within 1% of the experimental result. Using this validated technique a new pylon design was investigated to determine the influence the pylon can have. The new design reduced the drag for each design point by as much as five drag counts.

Design for manufacturing studies for engine nacelles and cost analysis were performed for engine nacelles in conjunction with trade off between manufacturing tolerances and aerodynamic tolerances and results were extrapolated to a complete aircraft. With a fuel price taken at US\$0.75 per gallon, the study resulted in approximately 1.3% DOC saving for a 2% saving in aircraft cost involving no drag rise, and additionally, approximately 0.4% DOC saving for a further 1% saving in aircraft cost for tolerance relaxation that did involve drag rise. The total of 1.7% DOC savings translates into savings of \$530 per sortie for the Airbus 320 class of aircraft. With a typical annual utilisation of 500 sorties that totals to \$265K per aircraft. For smaller aircraft the percentage savings could be higher.

## ACKNOWLEDGEMENTS

This paper is based on a collaborative research programme on Aircraft engine nacelle aerodynamics between the School of Mechanical and Aerospace Engineering at QUB and Bombardier, sustained over a ten year period and funded by Bombardier, the Department for Education and Learning, InvestNI, EPSRC and the Royal Academy of Engineering. The authors wish to acknowledge the contribution made during this period by researchers Dr Jeffrey Brown, Dr Kevin Donaghy, Dr Darren O'Neill, Dr Paul Humphries, Mr Peter Pratt, Dr Manuel Sanchez, Mr Ciaran Regan, Mr Rozli Zulkifli, Mr Stephen Crossby and Dr Ajay Kundu.

## REFERENCES

1. Federal Aviation Administration, Proceeding of the FAA International Conference on Aircraft In-Flight Icing, I and II, Springfield, Virginia, USA, 6-8 May 1996. Final Report.
2. United States Department of Transportation, Federal Aviation Administration, FAA In-Flight Icing Plan, April 1997.
3. THOMAS, S.K., CASSONI, R.P. and MACARTHUR, C.D. Aircraft anti-icing and deicing techniques and modeling. *AIAA J Aircr.* 33, (5), September-October 1996, pp 841-854.
4. BROWN, J.M., RAGHUNATHAN, S., WATTERSON, J.K., LINTON, A.J. and RIORDON, D. Heat transfer correlation for anti-icing systems. *AIAA J Aircr.* 39, (1), January-February 2002, pp 65-70.
5. JAMBUNATHAN, K., LAI, E., MOSS, M.A. and BUTTON, B.L. A review of heat transfer data for singular jet impingement. *Int J Heat and Fluid Flow*, 1992, 13, pp 106-115.
6. MARTIN, H. *Heat and mass Transfer between Impinging Gas Jets and Solid Surfaces*, Advances in Heat Transfer, 13, Academic Press, 1977, pp 1-60.
7. CORNARO, C., FLEISCHER, A.S. and GOLDSTEIN, R.J. Flow visualisation of a round jet impinging on cylindrical surfaces. *Experimental Thermal and Fluid Science*, 1999, 20, pp 66-78.
8. METZGER, D.E., YAMASHITA, T. and JENKINS, C.W. Impingement cooling of concave surfaces with high velocity impinging air jets. *J Eng for Power-Transactions of the ASME*, 1969, 91, pp 149-158.
9. DYBAN, E.P. and MAZUR, A.I. Heat transfer for a planar jet striking a concave surface, translated from *Inzhenerno-Fizicheskii Zhurnal*, 17, (5), November 1969, pp 785-790.

10. YEOMAN, E.K. Efficiency of a bleed air powered inlet icing protective system, 32nd Aerospace Sciences Meeting & Exhibit, AIAA Paper 94-0717, Reno, NV, USA, January 1994.
11. CROCE, G., HABASHI, W.G., GUÉVREMONT, G. and TEZOK, F. 3D thermal analysis of an anti-icing device using FENSAP-ICE, 36th Aerospace Sciences Meeting & Exhibit, AIAA Paper 98-0198, Reno, NV, USA, January 1998.
12. DE MATTOS, B. and S., OLIVEIRA, G.L. Three-dimensional thermal coupled analysis of a wing slice slat with a piccolo tube, 18th AIAA Applied Aerodynamics Conference, AIAA Paper 2000-3921, Denver, CO, USA, 14-17 August 2000.
13. MORENCY, F., TEZOK, F. and PARASCHIVOIU, I. Anti-icing system simulation using CANICE, *AIAA J Aircr*, 36, (6), November-December 1999, pp 999-1006.
14. MORENCY, F., TEZOK, F. and PARASCHIVOIU, I. Heat and mass transfer in the case of an anti-icing system modelisation, *AIAA J Aircr*, 37, (2), March-April 2000, pp 245-252. Also AIAA Paper 99-0623, January 1999.
15. MORENCY, F., TESSIER, P., SAEED, F. and PARASCHIVOIU, I. Anti-icing system simulation on multielement airfoil, CASI 46th Annual Conference/DNP-ASIP, Montréal, Canada, May 1999, pp 463-470.
16. TRAN, P., BRAHIMI, M.T., SANKAR, L.N. and PARASCHIVOIU, I. Ice accretion prediction on single and multi-element airfoils and the resulting performance degradation, 35th Aerospace Sciences Meeting & Exhibit, AIAA Paper 97-0178, Reno, NV, USA 6-9 January 1997.
17. TRAN, P., BRAHIMI, M.T., PARASCHIVOIU, I., PUEYO, A. and TEZOK, F., ice accretion on aircraft wings with thermodynamic effects, *AIAA J Aircr*, 1995, 32, (2), pp 444-446.
18. PARASCHIVOIU, I., TRAN, P. and BRAHIMI, M.T. Prediction of the ice accretion with viscous effects on aircraft wings, *AIAA J Aircr*, 31, (4), July-August 1994, pp 855-861.
19. TRAN, P., BRAHIMI, M.T. and PARASCHIVOIU, I. Ice accretion on aircraft wings, *Canadian Aeronautics and Space J*, September 1994, 40, (3), pp 185-192.
20. RUFF, G.A. and BERKOWITZ, B.M. User manual for the NASA Lewis ice accretion code prediction code LEWICE, NASA Contractor Report 185129, May 1990.
21. WRIGHT, W.B. User manual for the improved NASA Lewis ice accretion code LEWICE 1.6, NASA Contractor Report 198355, June 1995.
22. AL-KHALIL, K.M. Numerical simulation of an aircraft anti-icing system incorporating a rivulet model for the runback water, Ph.D. Thesis, University of Toledo, Ohio, USA, June 1991.
23. AL-KHALIL, K.M. and Potapczuk, M.G. Numerical modeling of anti-icing systems and numerical comparison to test results on a NACA 0012 Airfoil, 31st Aerospace Sciences Meeting & Exhibit, AIAA Paper 93-0170, Reno, NV, January 1993.
24. AL-KHALIL, K.M., FERGUSON, T.W. and PHILLIPS, D.M. A hybrid anti-icing ice protection system, 35th Aerospace Science Meeting & Exhibit, AIAA Paper 97-0302, Reno, NV, January 1997.
25. MEOLA, C., CARLOMAGNO, G.M., RIEGEL, E. and SALVATO, F. An experimental study of an anti-icing hot air spray-Tube System, 19th Congress ICAS, Anaheim, CA, September 1994.
26. Fregeau, Study and Simulation of the Ice accretion on aircraft and modeling of thermal anti-icing systems, M.S. Thesis, École Polytechnique de Montréal, Quebec, Canada, May 2004.
27. SAEED, F., MORENCY, F. and PARASCHIVOIU, I. Numerical simulation of a Hot-Air Anti-Icing Simulation, 38th Aerospace Sciences Meeting & Exhibit, AIAA Paper 2000-0630, Reno, NV, USA, January 2000.
28. SAEED, F. and PARASCHIVOIU, I. Numerical correlation for local Nusselt number distribution for hot-air jet impingement on concave surfaces, Proceedings of the 8th Annual Conference of the CFD Society of Canada, CFD2K, Montréal, Québec, Canada, 11-13 June 2000, 2, pp 897-904.
29. CROCE, G., BEAUGENDRE, H. and HABASHI, W.G. CHT3D: FENSAP-ICE Conjugate heat transfer computations with droplet impingement and runback water, 40th Aerospace Sciences Meeting & Exhibit, AIAA Paper 2002-0386, Reno, NV, USA, January 2002.
30. PUEYO, A., CHOCRON, D., MOKHTARIAN, F. and KAFYEKE, F. CHT2D: A 2D hot air anti-icing analysis tool, Proceedings of the 50th Annual General Meeting and Conference of CASI, Montreal, Canada, 28-30 April 2003.
31. MAVRIPLIS, D.J. and PIRZADEH, S. Large-scale parallel unstructured mesh computations for 3D high-lift analysis, ICASE Report No. 99-9, February 1999.
32. MAVRIPLIS, D.J. NSU3D (Version 3.4) A CFD package for external aerodynamics using an unstructured navier-stokes multigrid solver, Users Manual, Revision 2, September 2000.
33. MAVRIPLIS, D.J. and LEVY, D.W. Transonic drag prediction using an unstructured multigrid solver, 40th Aerospace Sciences Meeting & Exhibit, AIAA Paper 2002-0838, Reno, NV, USA, January 2002.
34. MAVRIPLIS, D.J. Aerodynamic drag prediction using unstructured solvers, VKI Lecture Notes for short course on CFD-Based Drag Prediction and Reduction, 3-7 February 2003, von Karman Institute for Fluid Dynamics, Rhode St Genese, Belgium.
35. IZZO, A.J. An experimental investigation of the turbulent characteristics of a boundary layer.
36. Flow over a vibrating plate – General Dynamics, Electric Boat Division – Contract NONR-2512(00) May 1969.
37. ROBINSON, S.K. Coherent motions in the turbulent boundary layer – *Ann Rev Fluid Mech*, 1991, 23, pp 601-639.
38. JUNG W.J., MANGIACACCHI N. and AKHAVAN R. Suppression of turbulence in wall bounded flows by high-frequency spanwise oscillations – *Phys. Fluids A*, 1992, (4), pp 1605-1607.
39. LAADHAR, F., SKANDAJI, L. and MOREL, R. Turbulence reduction in a boundary layer by a local spanwise oscillating surface – *Phys Fluids*, October 1994, 6, (10).
40. TRUJILLO, S.M., BOGARD, D.G. and BALL, K.S. Turbulent boundary layer drag reduction using an oscillating wall – AIAA Paper, 971870, 1997.
41. KENDALL, J.M. The turbulent boundary layer over a wall with progressive surface waves – *J. Fluid Mech*, 1970, 41, (2), pp 259-281.
42. KRAMER, M.O. Boundary layer stabilisation by distributed damping – *J. A. Soc Naval Engrs*, 1960, 72, pp 25-33.
43. GAD-EL-HAK, M. *Introduction to flow control – in flow control – fundamentals and practices*, GAD-EL-HAK, M., POLLARD, A., BONNET and J.P., (Eds), Springer Verlag, 1998, pp 1-107, 1998.
44. WILBY, J.F. and GLOYNA, F.L. Vibration measurements of an airplane fuselage structure – II. Jet Noise Excitation – *J Sound Vib*, 1972, 23, (4), pp 467-486.
45. MAESTRELLO, L. Design criterion of panel structure excited by turbulent boundary layer – *J Aircr*, July 1968, 5, (4), pp 321-328.
46. HUSSAIN A.K.M.F. and REYNOLDS W.C. The mechanics of an organised wave in turbulent shear flow – *J Fluid Mech.*, 41, (2), pp 241-258.
47. KLEBANOFF, P.S. Characteristics of turbulence in a boundary layer with zero pressure gradient – NACA Report 1247.
48. HAMA, R. Turbulent boundary layer along a flat plate I & II. – Rep Inst Science and Tech., Tokyo University, January 1947.
49. SCHULTZ-GRUNOW F. New frictional resistance law for smooth plates – NACA Report TM 986, 1941.
50. REGAN, C., BENARD, E., RAGHUNATHAN, S., RIORDAN, D. and LINTON, A., The effect of a wall normal vibration on a turbulent boundary layer, AIAA Paper 2002-0946, 40th AIAA Aerospace Sciences Meeting and Exhibit, 14-17 January 2002, Reno, NV, USA.
51. NEVINS, R.G. and BALL H.D. Heat transfer between a flat plate and a pulsating impinging jet, National Heat Transfer Conference Boulder, 1961, CO, ASME.
52. KATAOKA, K. and SUGURO, M. The effect of surface renewal due to large scale eddies on jet impingement heat transfer, *Int J Heat and Mass Transfer*, 1987, 30, pp 559-567.
53. SAILOR, D.J., DANIEL, J.R. and QIANLI, F. Effect of variable duty cycle flow pulsations on heat transfer enhancement for an impinging air jet, *Int J Heat and Fluid Flow*, 1999, 20, pp 574-580.
54. MLADIN, E.C. and ZUMBRUNNEN, D.A. dependence of heat transfer to a pulsating stagnation flow on pulse characteristics, *J Thermophysics and Heat Transfer*, 1995, 9, (1), pp 181-192.
55. ZUMBRUNNEN, D.A. and AZIZ, M. Convective heat transfer enhancement Due to intermittency in an impinging jet, *J Heat Transfer*, 1993, 115, pp 91-98.
56. AZEVEDO, L.F.A., WEBB, B.W. and QUEIROZ, M., Pulsed air jet impingement Heat Transfer, *Experimental Thermal and Fluid Science*, 1994, 8, pp 206-213.
57. FARRINGTON, R.B. and CLAUNCH, S.D. Infrared imaging of large amplitude, low frequency disturbances on a planar jet, *AIAA J*, 1994, 32, pp 317-323.
58. LIU, T. and SULLIVAN, J.P. Heat transfer and flow structures in an excited circular impinging jet. *Int J of Heat and Mass Transfer*, 39, (17), pp 3695-3706.
59. ZULKIFLI, R., BENARD, E., RAGHUNATHAN, S. and LINTON, A. Effect of pulse jet frequency on impingement heat transfer., AIAA 42th Aerospace Sciences Meeting, Reno, NV, USA, Paper 2004-1343.

60. LORD, M.W.K., MACMARTIN, P.G. and TILLMAN, T.G. Flow control opportunities in gas turbine engines, AIAA, 2000-2234, 2000.
61. POLAND, D.T. The aerodynamics of thrust reversers for high bypass Turbofans, AIAA, 67-418, July 1967.
62. YAO, H., BENARD, E., COOPER, R.K., RAGHUNATHAN, S., TWEEDIE, J. and RIORDAN, D. Aerodynamics of natural blockage thrust reverser, proceedings of CASI 50th AGM and Conference, 28-30 April, Montreal, QC, Canada, Paper 329, 2003.
63. KRAL, L.D. Recent experience with different turbulence models applied to the calculation of flow over aircraft components, *Progress in Aerospace Sciences*, 1998, 34, pp 481-541.
64. ROMINE, Jr B.M. and JOHNSON, W.A. Performance investigation of a fan thrust reverser for a high bypass turbofan engine, AIAA-84-1178, AIAA/SAE/ASME 20th Joint Propulsion Conference, Cincinnati, USA, June 1984.
65. YAO, H., BUTTERFIELD, J., RAGHUNATHAN, S., COOPER, R. and BENARD, E. Optimization design for thrust reverser cascade with a view to Reduce Noise, Accepted for publication in *Int J Multidiscipline Modeling in Materials and Structures*.
66. YAO, H., BUTTERFIELD, J. and RAGHUNATHAN, S. The aerodynamic performance of thrust reverser cascade, Proceeding of the 24th International Congress of Aeronautical Sciences (ICAS 2004), ICAS 2004-4.2.R, Yokohama, Japan, August 2004.
67. YAO, H., BENARD, E., CURRAN, R., PRICE, M., ARMSTRONG, C.G. and RAGHUNATHAN, S. Integration of aerodynamic, structural, cost and manufacturing considerations during the conceptual design of a thrust reverser cascade, AIAA Paper 2004-1239, 42nd AIAA Aerospace Sciences Meeting and Exhibit, Reno, Nevada, USA, January 2004.
68. HALL, S., YAO, H., COOPER, R.K., BENARD, E. and RAGHUNATHAN, S. Experimental investigation of a cascade thrust reverser, 9th Aerodynamics Symposium, 239b, Montreal, Canada, 2003.
69. HALL, S., BENARD, E. and RAGHUNATHAN, S. Progress in developing innovative flow control in a cascade thrust reverser, 24th International Congress of the Aeronautical Sciences, 2004.
70. YAO, H., BENARD, E., COOPER, R. K., RAGHUNATHAN, S., TWEEDIE, J. and RIORDAN, D. Aerodynamics of natural blockage thrust reverser, 9th Aerodynamics Symposium, Montreal, Canada, 28-30 April 2003.
71. BUTTERFIELD, J., YAO, H., PRICE, M., RAGHUNATHAN, S. and ARMSTRONG, C. Methodologies for structural optimisation of a thrust reverser cascade, AIAA Paper 2003-0107, 41st AIAA Aerospace Sciences Meeting and Exhibit, 6-9 January 2003, Reno, NV, USA.
72. BUTTERFIELD, J., YAO, H., BENARD, E., PRICE, M., COOPER, R., MONAGHAN, D., ARMSTRONG, C.G. and RAGHUNATHAN, S. Optimisation of thrust reverser cascade performance using aerodynamic and structural integration. Proceedings of CEAS Aerospace Aerodynamics Research Conference, 10-12 June, 2003, Royal Aeronautical Society, London.
73. BUTTERFIELD, J., YAO, H., BENARD, E., PRICE, M., COOPER, R., MONAGHAN, D., ARMSTRONG and C.G., RAGHUNATHAN, S. Investigation of weight reduction in a thrust reverser Cascade Using Aerodynamic and Structural Integration. AIAA Paper 2003-1576, 44th AIAA/ASME/AHS Structures, Structural Dynamics and Materials Conference, 7-10 April, 2003, Norfolk, Va, USA.
74. BUTTERFIELD, J., YAO, H., BENARD, E., PRICE, M., COOPER, R., MONAGHAN, D., ARMSTRONG, C.G. and RAGHUNATHAN, S. Optimisation of a thrust reverser cascade: An assessment of dynamic response with a view to reducing weight. AIAA Paper 2003-6748, 3rd Annual Aviation Technology, Integration and Operations (ATIO) Technical Forum, 17-19 November 2003, Denver, Colorado, USA.
75. BUTTERFIELD, J., YAO, H., CURRAN, R., PRICE, M., ARMSTRONG, C.G. and RAGHUNATHAN, S. Integration of aerodynamic, structural, cost and manufacturing considerations during the conceptual design of a thrust reverser cascade. AIAA Paper 2003, 42nd AIAA Aerospace Sciences Meeting and Exhibit, 5-8 January 2004.
76. YAO, H., RAGHUNATHAN, BENARD, E. and COOPER, R. Numerical simulation of natural blockage thrust reverser. AIAA 43rd Aerospace Sciences meeting, Reno Nevada, USA, January 2005. Paper 2005-0631.
77. BUTTERFIELD, J., YAO, H., PRICE, M., BENARD, E., COOPER, R., MONAGHAN, D., ARMSTRONG, C. and RAGHUNATHAN, S. Enhancement of thrust reverser cascade performance using aerodynamic and structural integration, *Aeronaut J* 2004, 108, (1090), pp 621-628.
78. DONAGHY, K. Fire Propagation and Heat transfer Modelling Within The BR710 Nacelle for Certification Purposes, PhD thesis, Queens University Belfast, 2000.
79. DONAGHY, K., RAGHUNATHAN, S. and RIORDAN, D. Fire zone modelling of aircraft engines, 37th AIAA Aerospace Sciences Meeting, 1999, Paper 99- 0236, Reno, NV, USA.
80. DEVINE, R.J. WATTERSON, J.K. and COOPER, R.K. Performance improvement of flush, parallel walled auxiliary intakes by means of vortex generators, 24th International Congress of the Aeronautical Sciences, Paper ICAS2004-4.2.3, August 2004, Japan.
81. DEVINE, R.D. The Performance of Nacelle Ventilation Intakes at Low Speed, PhD thesis, Queens University Belfast, 2003.
82. PRATT, P., WATTERSON, J.K. and BENARD, E., Performance of a flapped duct exhausting into a compressible external flow, 24th International Congress of the Aeronautical Sciences, Paper ICAS2004-04.2.R, August 2004, Japan. Augustine, N. *Autustine Laes*, 6th Edition, AIAA, Reston, VA, 1997.
83. Federal Aviation Administration, General guidelines for measuring fire-extinguishing agent concentration in powerplant compartments, Advisory Circular, AC No 20-100, 1977.
84. United Nations, Report of the Halon Fire Extinguishing Agents Technical Options Committee, United Nations Environment Programme (UNEP), 1994.
85. PITTS, W., NYDEN, M., GANN, R., MALLARD, W. and TSANG, W. Construction of an exploratory list of chemicals to initiate the search for Halon alternatives, NIST TN-1279, National Institute of Standards and Technology, 1990.
86. GROSSHANDLER, W., GANN, R. and PITTS, W. (Eds) Evaluations of alternative in-flight fire suppressants for full-scale simulated aircraft engine nacelles and dry bays. SP-861, National Institute of Standards and Technology, 1994.
87. GANN, R. (Ed), Fire suppression system performance of alternative agents in aircraft engine and dry bay laboratory simulations, SP-890, National Institute of Standards and Technology, 1995.
88. HAMINS, A., CLEARY, T., BORTHWICK, P., GORCHKOV, N., MCGRATTAN, K., FORNEY, G., GROSSHANDLER, W., PRESSER, C. and MELTON, L. Suppression of engine nacelle fires, fire suppression system performance of alternative agents in aircraft engine and dry bay laboratory simulations, edited by GANN, R., Vol 2 of SP-890, chap. 9, National Institute of Standards and Technology, 1995, pp 1-199.
89. LOPEZ, A., GRITZO, L. and HASSAN, B. Computational fluid dynamics simulation of the air/suppressant flow in an uncluttered F18 engine nacelle, Proc. Halon Options Tech. Working Conference, Albuquerque, New Mexico, USA, 1997, pp 281-297.
90. NICOLETTE, V., LOPEZ, A. and GRITZO, L. F18 Nacelle fire simulation, Sandia National Laboratories Technical Memorandum to Leo Budd, 1997.
91. VICK, A.R. An investigation of discharge and thrust characteristics of flapped outlets for stream Mach numbers from 0.4 to 1.3, NACA TN-4007, 1957.
92. ACARE. European Aeronautics: A vision for 2020 – meeting society's needs and winning global leadership, Report of the group of personalities, January 2001.
93. BARRY, B., PARKE, S.J., BOWN, N.W., RIEDEL, H. and SITZMANN, M. Flight testing of natural and hybrid laminar flow nacelles, ASME Proceedings of the International Gas Turbine and Aeroengine Congress and Exposition, 13-16 June 1994, Hague, Neth, ASME 94 -GT-408.
94. BRODERSEN, O. Drag prediction of engine-airframe interference effects using unstructured Navier-Stokes calculations, *J Aircr*, 2002, 39, (6), 2002, pp 927-935.
95. ROSSOW, C.C., GODARD, J.-L., HOHEISEL, H. and SCHMITT, V. Investigation of repulsion integration interference effects on a transport aircraft configuration, *J Aircr*, 1994, 31, (5), pp 1022-1030.
96. HENDERSON, W.P., Airframe/Propulsion Integration at Transonic Speeds, *J Engineering for Gas Turbines and Power*, Transactions of the ASME, v 113, n 1, January 1991, pp 51-59.
97. GODARD, J.L., HOHEISEL, H., ROSSOW, C.C. and SCHMITT, V. Investigation of Interference Effects for Different Engine Positions on a Transport Aircraft Configuration, *Proceedings of DLR Workshop on Aspects of Engine Airframe Integration For Transport Aircraft*, edited by H. HOHEISEL, German Aerospace Research Centre, DLR, TR 96-01, Brunswick, Germany, 1996, pp 11.1-11.22.
98. BERRY, D. The Boeing 777 engine/airframe integration aerodynamics design process, international council of the aeronautical sciences, 94-6.4.4, September 1994.
99. RUDNIK, R. and ROSSOW, C.C. Numerical simulations of engine/airframe integration for high-bypass engines, ECCOMAS – 2000 Paper, 2000.
100. INGRALDI, A.M., KARIYA, T.T., RE, R.J. and PENDERGRAFT, O.C. Interference effects of very high bypass ratio nacelle installations on a low-wing transport, *J Engineering for Gas Turbines and Power*, Transactions of the ASME, v 114, 4, October 1992, pp 809-815.



101. ROSSOW, C.C. and HOHEISEL, H. Numerical study of interference effects of wing-mounted advanced engine Concepts, International Council of the Aeronautical Sciences, 94-6.4.1, September 1994.
102. JIE, LI., FENGWEI, LI. and QIN, E. Numerical simulation of transonic flow over wing-mounted twin-engine transport aircraft, *J Aircraft*, 2000, 37, (3), pp 469-478.
103. RUDNIK, R., ROSSOW, C.C. and v. GEYR, H.F. Numerical simulations of engine/airframe integration for high-bypass engines, *Aerospace Science and Technology*, 2002, 6, pp 31-42.
104. MURMAN, E.M., WALTON, M. and REBENTISCH, E. Challenges in better, faster, cheaper era of aeronautical design, engineering and manufacturing, *Aeronaut J*, Oct 2001, pp 481-489.
105. KUNDU, A., RAGHUNATHAN, S. and MORRIS, W. Effect of manufacturing Tolerances on aircraft aerodynamics and cost world manufacturing congress. New Zealand, November 1997. Paper 711-003.
106. KUNDU, A., RAGHUNATHAN, S. and COOPER, R.K. Effect of aircraft smoothness requirements on cost, *Aeronaut J*, December 2000, 104, (1039), Paper 2389, pp 415-420.
107. CURRAN, R., KUNDU, A., RAGHUNATHAN, S. and McSPADDEN, R. Impact of the aerodynamic surface tolerance on aircraft cost driver, *J aerospace engineering*, Proc of the IMechE, Part C, 215, 2001, pp 29-39.
108. CURRAN, R., KUNDU, A., RAGHUNATHAN, S. and EAKIN, D. Costing tools for decision making within integrated aerospace design, concurrent engineering: research and applications, 2001, 9, (4), pp 327-338.
109. KUNDU, A., WATTERSON, J.K., RAGHUNATHAN, S. and McFADDEN, R. Parametric optimisation of manufacturing tolerances at the aircraft surface, *J Aircr*, AIAA, 2002, 39, (2), pp 271-279.
110. CURRAN, R., KUNDU, A., RAGHUNATHAN, S. and McFADDEN, R. Influence of manufacturing tolerance on aircraft direct operating cost (DOC), *J Materials Processing Technology*, Elsevier Science B.V., ISSN: 0924-0136, 138, 2002, pp 208-213.
111. SANCHEZ, M., KUNDU, A.K., HINDS, B.K. and RAGHUNATHAN, S. A methodology for assessing manufacturing cost due to tolerance on aerodynamic surface features on turbo fan nacelles, international J advanced manufacturing Technology, 1999, 14, pp 894-900.